Fingerprints of spin-orbital polarons and of their disorder in the photoemission spectra of doped Mott insulators with orbital degeneracy

Adolfo Avella,[1,2,3] Andrzej M. Oleś,[4,5] and Peter Horsch[5]
[1]*Dipartimento di Fisica "E.R. Caianiello," Universitá degli Studi di Salerno, I-84084 Fisciano (SA), Italy*
[2]*CNR-SPIN, UoS di Salerno, I-84084 Fisciano (SA), Italy*
[3]*Unità CNISM di Salerno, Università degli Studi di Salerno, I-84084 Fisciano (SA), Italy*
[4]*Marian Smoluchowski Institute of Physics, Jagiellonian University, Prof. S. Łojasiewicza 11, PL-30348 Kraków, Poland*
[5]*Max-Planck-Institut für Festkörperforschung, Heisenbergstrasse 1, D-70569 Stuttgart, Germany*

(Received 28 July 2017; revised manuscript received 1 February 2018; published 4 April 2018)

We explore the effects of disordered charged defects on the electronic excitations observed in the photoemission spectra of doped transition metal oxides in the Mott insulating regime by the example of the $R_{1-x}Ca_xVO_3$ perovskites, where $R = \mathrm{La}, \ldots, \mathrm{Lu}$. A fundamental characteristic of these vanadium d^2 compounds with partly filled t_{2g} valence orbitals is the persistence of spin and orbital order up to high doping, in contrast to the loss of magnetic order in high-T_c cuprates at low defect concentration. We study the disordered electronic structure of such doped Mott-Hubbard insulators within the unrestricted Hartree-Fock approximation and, as a result, manage to explain the spectral features that occur in photoemission and inverse photoemission. In particular, (i) the atomic multiplet excitations in the inverse photoemission spectra and the various defect-related states and satellites are qualitatively well reproduced, (ii) a robust Mott gap survives up to large doping, and (iii) we show that the defect states inside the Mott gap develop a soft gap at the Fermi energy. The soft defect-states gap, which separates the highest occupied from the lowest unoccupied states, can be characterized by a shape and a scale parameter extracted from a Weibull statistical sampling of the density of states near the chemical potential. These parameters provide a criterion and a comprehensive schematization for the insulator-metal transition in disordered systems. Our results provide clear indications that doped holes are bound to charged defects and form small spin-orbital polarons whose *internal* kinetic energy is responsible for the opening of the soft defect-states gap. We show that this *kinetic* gap survives disorder fluctuations of defects and is amplified by the long-range electron-electron interactions, whereas we observe a Coulomb singularity in the atomic limit. The small size of spin-orbital polarons is inferred by an analysis of the inverse participation ratio and by means of a complementary many-body polaron theory, which yields a similar robust spin and orbital order as the Hartree-Fock approximation. Using realistic parameters for the vanadium perovskite $La_{1-x}Ca_xVO_3$, we show that its soft gap is reproduced as well as the marginal doping dependence of the position of the chemical potential relative to the center of the lower Hubbard band. The present theory uncovers also the reasons why the $d^1 \rightarrow d^0$ satellite excitations, which directly probe the effect of the random defect fields on the polaron state, are not well resolved in the available experimental photoemission spectra for $La_{1-x}Ca_xVO_3$.

DOI: 10.1103/PhysRevB.97.155104

I. INTRODUCTION

In this work, we deal with transition metal oxides that are in their intrinsic state Mott insulators as a result of strong electron-electron (e-e) repulsion and not band insulators as semiconductors [1,2]. Mott insulating materials typically display different realizations of quantum magnetism and some of them realize rare quantum spin-liquid states [3–6]. Doping Mott insulators can have striking consequences. For example, doping the two-dimensional (2D) antiferromagnetic (AF) Mott insulator La_2CuO_4 with Sr, Ba, or Ca gives rise to high-T_c superconductivity [7–10], with an insulator to superconductor transition and the disappearance of AF order at very low doping [11–13]. Manganites are paradigmatic examples of systems characterized by spin, orbital, and charge degrees of freedom that are controlled by spin-orbital superexchange interactions [14–19]. Doping the Mott insulator $LaMnO_3$, for instance, leads to a variety of insulating spin-, orbital-, and charge-ordered phases [20–26], as well as to a metallic regime that displays a colossal magnetoresistance [27–29].

A very interesting class of materials where the orbital degree of freedom plays an important role are the $3d$-electron systems with active t_{2g} degrees of freedom that favor orbital fluctuations [17,30]. In the titanium perovskites, they play a prominent role in the spin-orbital ordered states or may even trigger a disordered state [31–36], while superconductivity was discovered at $SrTiO_3$ interfaces [37–40]. We shall focus here on the vanadium perovskites RVO_3, where $R = \mathrm{La}, \ldots, \mathrm{Lu}$, which reveal temperature-induced magnetization reversals [41] as a result of the coupling of spin and orbital degrees of freedom of the t_{2g} valence electrons [42–47]. This class of compounds has interesting phase diagrams with two complementary spin-orbital ordered phases and a pure orbital-ordered phase [48–54]. Remarkably, the C-type spin and G-type orbital ordered phase in $La_{1-x}Sr_xVO_3$, $Pr_{1-x}Ca_xVO_3$ and $Y_{1-x}Ca_xVO_3$

is robust up to high-doping concentrations and also the metal-insulator transition takes place only at quite substantial doping [55–58]. This striking robustness of the spin-orbital ordered state against doping as compared to the fragile AF state in the cuprates is one of the motivations for this work.

The combination of spin and orbital degrees of freedom triggers spin-orbital (SO) polarons [59–62]. We shall discuss in this work why small SO polarons in the insulating regime of cubic vanadates [58,63] are much more strongly bound to charged defects than spin polarons in high-T_c materials [64,65]. The reduced mobility of doped holes or electrons inside the SO polarons implies a weaker screening of defect potentials by the doped charge carriers and thus provides an explanation for the shift of the insulator to metal transition towards high doping concentrations in the vanadates. Here, we shall support these conclusions by a careful analysis of the doping dependence of the density of states, i.e., of photoemission (PES) and inverse photoemission (IPES) spectra. We explore the localization of defect-states wave functions, the defect-states gap inside the Mott-Hubbard (MH) gap, and finally the reduction of spin and orbital order and its relation to the many-body SO polaron wave function and the binding to defects.

The cubic vanadates represent a class of compounds with quantum fluctuating orbitals and spins, even in the absence of doping. In contrast to the manganites, the cubic vanadates have very small Jahn-Teller interactions due to the t_{2g} nature of their valence electrons. Therefore, orbital occupations are not rigid even in the ordered phases, but fluctuate [43,44,66]. Several peculiar features can be traced back to orbital quantum fluctuations, such as ferromagnetism driven by orbital singlet fluctuations [43] and orbital Peierls dimerization [44–47]. Indeed, the joint spin and orbital fluctuations are particularly strong in the ordered C-type AF and G-type alternating orbital (AO) phase, i.e., C-AF/G-AO phase, realized in these compounds when they are doped [67]. Furthermore, it was shown that charged defects tend to enhance orbital Peierls dimerization [67]. An important motivation for the investigation of cubic vanadates is a large experimental data base for these systems, which includes the phase diagrams of many undoped compounds [48–50] and their pressure dependence [68], as well as the doping dependence of the optical conductivity for several systems [57]. In this work, our focus is on the doping dependence of the PES spectra of the vanadium perovskites [69–71].

Solving this problem involves answering questions like: (i) what is the nature of defect states in a strongly correlated system, i.e., to what extent are such defect states different from those in usual semiconductors or band insulators [72,73]? (ii) What happens to the MH gap in the presence of defects? (iii) Which are the different features of defect states in MH insulators with t_{2g} orbital degeneracy as compared to those in doped high-T_c superconductors? (iv) Which methods, among those capable to yield reliable results for MH insulators, can be efficiently extended to take into account defects and disorder? To answer these questions is a formidable challenge, as defects greatly influence the subtle interplay of spin, orbital, lattice and charge degrees of freedom.

The calculation of the electronic structure of a disordered system with charged defects and long-range e-e interactions is a difficult optimization problem even for the simplest models for the defect states in the gap of semiconductors, e.g., the Coulomb glass (CG) model [72]. The effect of disorder and the resulting localization of electron states has a long history [74,75]. The reason for the calculational complexity of the insulating phase is the absence of metallic screening, and therefore the energy and occupation of a defect state depends on that of far distant random defects because of the long-range Coulomb interaction [75]. In contrast, in the metallic state, because of the presence of a Fermi surface, perturbative diagrammatic techniques can be applied to deal with multiple scattering corrections leading to a Coulomb anomaly in the density of states (DOS) $N(\omega)$ [76]. For the insulating phase, it was argued by Pollak [77] that e-e interactions should lead to a depletion of $N(\omega)$ at the chemical potential in systems with disorder. For the CG model, Efros *et al.* [78–80] could show, using some simplifying criteria, that the Coulomb interaction generates a soft gap at the chemical potential in $N(\omega) \propto |\omega|^{\nu}$, with an exponent $\nu = d - 1$ determined by the spatial dimension d. This is called the Coulomb gap [78]. Recently, Shinoaka and Imada [81,82] reported unconventional soft gaps for models with only short-range interactions. Furthermore, a disorder-induced Coulomb or zero-bias anomaly was observed by Epperlein *et al.* [83] for the quantum CG model and by Yun Song *et al.* [84] for an extended Anderson-Hubbard model.

We base our study on a generic spinful three-band model for the t_{2g} electrons on the vanadium ions [63] that provides a complete description of the magnetic and orbital ordered phases. The model includes the local Hubbard-Hund interactions and thereby describes the atomic multiplet structure of the V ions. Moreover, the model contains the long-range e-e interactions, and thereby it includes the dielectric screening of the t_{2g} electrons, and the Coulomb potentials of the random defects. Finally, there is the flavor conserving kinetic energy of t_{2g} electrons, and moreover crystal field and Jahn-Teller interactions. All these interactions together yield spin-orbital superexchange and pure orbital interactions that determine the different spin and orbital ordered phases [43,66]. This model can be simplified by the elimination of degrees of freedom and by the removal of terms, such as the kinetic energy or the Hubbard interaction, for instance, to obtain simpler models that have been used in the study of disorder. For instance, one may arrive at the CG [78] or at the quantum CG [77,83] models after elimination of spin and orbital degrees of freedom, or at the Anderson-Hubbard model [81] after elimination of the orbital degrees of freedom, see Fig. 1.

To analyze systems with defects and disorder, one needs to use a computationally efficient approach as averaging over several defect realizations and dealing with large inhomogeneous systems is necessary. Examples of such approaches are Hartree and the Hartree-Fock approximations [65,67,85–87], and the density functional theory [88–90]. Besides disorder, the calculations of the electronic structure and excitations of the spinful multiband models with charged defects are complicated by the fact that these systems are Mott insulators. We have pointed out before that the Hartree-Fock method is also capable to describe faithfully the high-spin excitations in the spin-orbital degenerate case provided the system has a broken spin and/or orbital symmetry [67,91]. However, low spin excitations are only qualitatively correct in Hartree-Fock and require

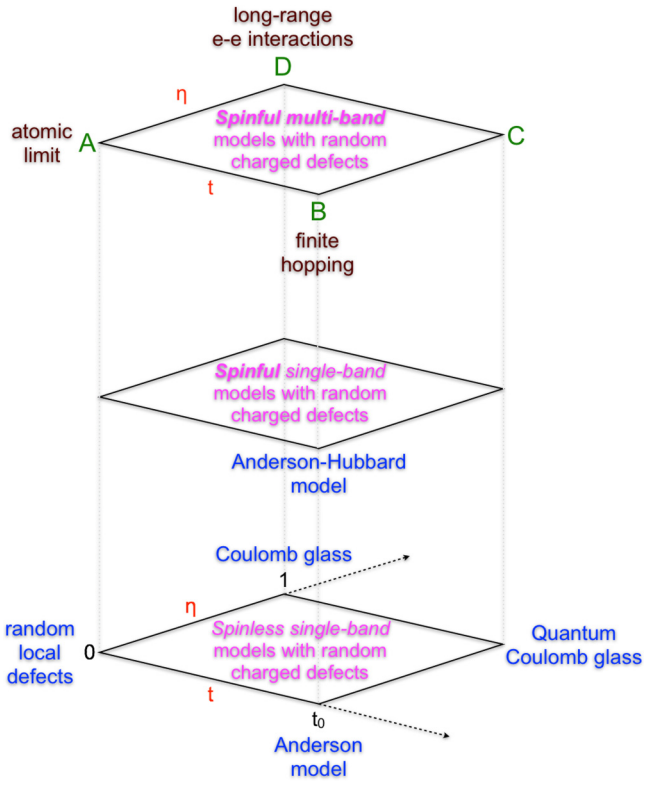

FIG. 1. Schematic hierarchy of typical models for systems with disorder. On the lowest level, generic models with a single orbital per site and no spin are shown. These models are further distinguished depending on whether they involve long-range e-e interactions (η scale) and/or kinetic energy (t scale). By adding spin to charge carriers, one finds single-orbital Hubbard-type models shown on the second level. On the third top level, reside models with spin and orbital degrees of freedom of interest for this paper, designed for doped spin-orbital systems. The labels A, B, C, and D refer to models explained and investigated in the following sections.

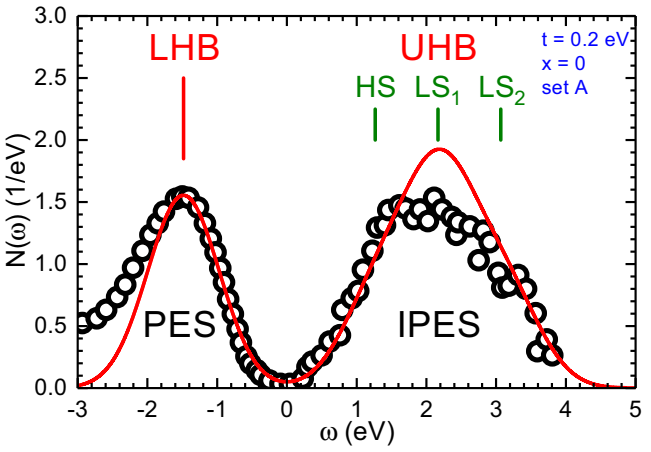

FIG. 2. Photoemission (PES) and inverse photoemission (IPES) spectra for undoped $LaVO_3$ in the vicinity of the chemical potential, which is located at $\omega = 0$. Experimental data (black hollow circles) were obtained by Maiti and Sarma [70]; the solid (red) curve was obtained from the theory reported in Sec. IV, with the three peaks of the UHB marked as HS, LS_1, and LS_2 standing for the high-spin and the two low-spin excitations, respectively.

quantitative corrections by Hund's exchange element J_H. In presence of local off-diagonal terms, the Hubbard-Hund interaction has to be expressed in a rotational invariant form in spin and orbital space. The unrestricted Hartree-Fock (uHF) method [92–94] is known to be reliable for systems with spontaneously broken symmetries as, for instance, multiband models for manganites [85,95], or the iron-based superconductors [96–99] or clusters of transition metals with magnetic ground states [86]. The uHF method designed and used in this paper is capable to treat simultaneously phenomena that arise at distinct energy scales: the high energy scale of $\sim$1 eV related to the (on-site and intersite) Coulomb interactions in proximity of the defects and the low energy scale of $\sim$0.1 eV that is characteristic of the orbital physics and controls the electronic transport in doped materials. Accordingly, the method is able to address the onset of the spin and orbital orders and their remarkable robustness in doped $La_{1-x}Sr_xVO_3$ and $Y_{1-x}Ca_xVO_3$.

Figure 2 displays PES and IPES data of Maiti and Sarma [70] for the undoped reference compound $LaVO_3$. The data provide evidence that the system is a Mott insulator. One recognizes the lower Hubbard band (LHB) in PES and one also sees the upper Hubbard band (UHB) in IPES, where the theoretically expected multiplet bands have some correspondence with features in the experiment. The fact that the Hubbard gap in the vicinity of $\omega = 0$ appears as a soft gap suggests that the sample contained possibly some defects at the surface [65]. The experimental data are compared with the uHF calculation, where the DOS $N(\omega)$ is broadened with an extra linewidth of $\gamma = 0.5$ eV. This has the consequence that the multiplets of the UHB are no longer resolved in the theoretical DOS $N(\omega)$.

A surprising feature of the electronic structure of cubic vanadates is the persistence of the MH gap up to high doping concentrations [67]. This has been demonstrated most clearly by optical conductivity experiments [57] in $La_{1-x}Sr_xVO_3$ and $Y_{1-x}Ca_xVO_3$ for doping concentrations up to $x = 0.1$ and 0.17, respectively. Our uHF calculations of the statistically averaged DOS $N(\omega)$ reproduce this robustness of the MH bands beyond doping concentrations of 50%, despite the fact that substantial spectral weight is transferred from the Hubbard bands to defect states. The latter appear as satellites and as states inside the MH gap. We shall discuss the energetics of these states, the sum rules, and the spectral weight transfers.

Our main focus is on the defect states that appear in the MH gap and that themselves form a *defect-states (DS) gap* at the chemical potential. The DS gap depends both on the kinetic energy parameter t and the e-e interaction strength, which we can tune with a coupling constant $\eta \in [0,1]$, where $\eta = 0$ corresponds to the absence of e-e interactions and $\eta = 1$ to the estimated typical strength for these interactions in vanadates. We perform a statistical analysis of the power law behavior of the DS gap in the DOS $N(\omega) \propto |\omega|^{\nu}$ in the vicinity of the chemical potential. The exponent ν is nonuniversal and depends on t and η. It is shown that the kinetic energy of the t_{2g} electrons plays a fundamental role for the formation of the DS gap in the cubic vanadates [63]. This mechanism is distinct from the Coulomb gap mechanism. We furthermore show that, with increasing η, e-e interactions of Coulomb type do increase the DS gap. Yet in the atomic limit, that is without

kinetic energy ($t = 0$), we found that *e-e* interactions alone are not strong enough in the cubic vanadates to open a Coulomb gap.

We investigate the localization of defect states by means of the inverse participation number (IPN) [100–102]. We have generalized this concept here to the case with spin- and orbital- degeneracy. We find that, at moderate doping, all wave functions are well localized. The states in the Hubbard bands are less localized than the defect states inside the Mott gap that contribute to the soft gap. These states are typically localized on 1–2 sites with tiny admixtures from further neighbors. Interestingly, we observe a discontinuity in the localization of the wave functions below and above the chemical potential when *e-e* interactions are switched on. The small participation number (<2) for the doped hole states can be taken as an unambiguous sign that holes are in small *spin-orbital polaron states* that are strongly bound to the charged defects, i.e., basically on a single bond. This leads to a reduction of spatial symmetry [63]. The strong localization of wave functions appears consistent with experiments by Nguyen and Goodenough [103], who analyzed the magnetic properties of the $La_{1-x}Ca_xVO_3$ system and concluded that carriers reside in trapped small-polaron states. Moreover, in a recent combined x-ray and neutron diffraction study of $Pr_{1-x}Ca_xVO_3$, Reehuis *et. al.* [58] found signatures of spin-orbital polarons from the change of spin and orbital correlations close to the insulator-metal transition at $x \simeq 0.23$.

In PES experiments of gapped systems, the position of the chemical potential μ is a subtle issue as it is determined by defects [104,105]. For the doped cubic vanadates, we find that μ lies in the center of the DS gap that forms inside the MH gap. We find that the distance of μ from the center of the LHB scales with the binding strength of the Ca defect and is basically unchanged by doping up to 50%, consistent with the PES study of Maiti and Sarma [69,70] for $La_{1-x}Ca_xVO_3$. We interpret this as manifestation of small polaron physics. Furthermore, we show that $d^1 \rightarrow d^0$ satellites in PES spectra can provide a precise fingerprint of the state of spin-orbital polarons and the strength and variance of the random defect fields acting on it.

The paper is organized as follows. In Sec. II, we introduce the triply degenerate Hubbard model for t_{2g} electrons in the doped perovskite vanadates, such as $La_{1-x}Ca_xVO_3$ with Ca^{2+} charged defects replacing randomly some La^{3+} ions. The model includes local (on-site) and long-range Coulomb interactions, as well as the Coulomb potentials induced by Ca defects, which increase the energies of the t_{2g} electrons located close to the defects taking also into account the contributions of more distant defects at random positions. We treat the *e-e* interactions in the uHF approximation and consider two parameter sets for $La_{1-x}Ca_xVO_3$ motivated by the experimental data in Sec. III. Using this approach and performing self-consistent calculations for realistic t_{2g} hopping integral, $t = 0.2$ eV, we obtained the one-particle DOSs presented in Sec. IV A. They are interpreted using the generic structure of the PES and IPES spectra in a doped system with orbital degeneracy derived from the atomic limit in Sec. IV B. We analyze the multiplet structure and comment on the PES and IPES data obtained for the undoped $LaVO_3$ [70]. The numerical spectral weights near the atomic limit confirm the exact calculations, as shown in Sec. IV C. Furthermore, using the results simulating the atomic limit (i.e., for a very low value of the hopping integral $t = 0.01$ eV) we extract the effects that arise due to finite kinetic energy and emphasize the role played by active bonds in Sec. IV D. While the excitations related to the active bonds can be resolved from the spectra, we also analyze the sum rules obeyed by the structures seen in the PES. In Sec. V, we elucidate the kinetic mechanism behind the DS gap in the present system and perform the Weibull analysis [63]. The electronic states that contribute to the spectral functions have various degrees of localization, which are universal for various defect realizations, as we show in detail in Sec. VI. Actually, more localized states appear at the edges of Hubbard bands. In Sec. VII, we explain the gradual changes of spin-orbital order with increasing doping within the polaron picture. Finally, in Sec. VIII, we address the experimental results for PES and IPES in doped systems and suggest that the large defect potential is responsible for the overall scenario, which is consistent with the experiments for $La_{1-x}Ca_xVO_3$. The final discussion and summary are presented in Sec. IX. The technical details of the present calculations are reported in two appendices; in Appendix A, one finds a general discussion of the algorithm for a system with random defects, while in Appendix B, it is explained what one can learn by a perturbative analysis in terms of spin-orbital polarons.

II. MOTT INSULATOR WITH CHARGED DEFECTS

We shall describe the doped $R_{1-x}Ca_xVO_3$ compounds (here R stands either for yttrium Y or for lanthanum La) by means of a multiband Hubbard model describing the subspace of t_{2g} states at vanadium ions. Previous studies [17,18,43,44,106] have shown that t_{2g} orbitals are crucial for the description of the perovskite vanadates as Mott insulators. Each dopant—calcium Ca^{2+} ions randomly replacing Y^{3+} or La^{3+}ions in this specific case—is equivalent to an effective charged defect sourcing a long-range Coulomb potential. The degree of randomness of the dopants' locations is controlled, in principle, by the annealing procedure used (or not used: full randomness as in the case we analyze here) during the fabrication of the samples and leads to a quite general disorder problem in the Mott insulating regime. The sequence of terms in the following Hamiltonian is selected to highlight the crucial role played by the charged defects and the long-range *e-e* interaction in the present system [63],

$$\mathcal{H}_{t_{2g}} = \sum_i h_i n_i + \frac{1}{2}\sum_{i\neq j} V_{ij} n_i n_j + \mathcal{H}_{\rm kin} + \mathcal{H}_{\rm int} + \mathcal{H}_{\rm CF} + \mathcal{H}_{\rm JT}, \qquad (2.1)$$

where $n_i = \sum_{\alpha\sigma} n_{i\alpha\sigma}$ and $n_{i\alpha\sigma} = d^\dagger_{i\alpha\sigma} d_{i\alpha\sigma}$ are the electron density operator and the partial electron density operator for orbital α and spin $\sigma = \uparrow,\downarrow$, respectively, at site i of a cubic Bravais lattice.

If we would restrict the Hamiltonian (2.1) to the single-orbital case, the first two terms would represent the CG model [78] with randomly distributed local levels $\{h_i\}$ and long-range *e-e* interactions of Coulomb type. A very important difference though between the model we propose and those usually encountered in the literature resides in the realization of the disorder: we use a fully random distribution of charged defects

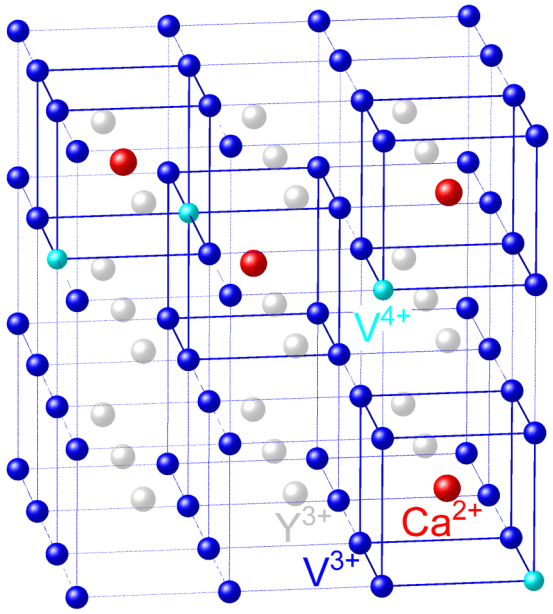

FIG. 3. Cubic vanadium lattice of the doped perovskite vanadate compound $R_{1-x}Ca_xVO_3$ with random Ca^{2+} defects replacing Y^{3+} ions (O-ions are not shown). Doped holes occupy V^{4+} ions in the cubic V^{3+} lattice and are attracted by the Ca^{2+} ions on the cubes surrounding the defects.

leading to a realistic distribution of energy levels that depends on the analyzed crystal structure and on the level of doping, and is very structured, that is, very far from the uniform or Gaussian distributions usually used [see Fig. 14]. The additional inclusion of a nearest-neighbor hopping term would lead to the quantum CG [77,83]. Without long-range *e*-*e* interactions, but with a finite nearest-neighbor hopping term between random levels, one would instead get the Anderson model, see Fig. 1. The strongly correlated cousins of these models involve in addition the local Hubbard interaction between electrons with opposite spins that could lead to the opening of a Mott gap. One representative model of this class is the Anderson-Hubbard model [81] that belongs to the next level of sophistication in the hierarchy of models with disorder, see Fig. 1.

As we shall see below in greater detail than what already announced above, crucial to our analysis are the random fields,

$$h_i = \sum_m V_{im}^{\rm D}, \tag{2.2}$$

due to the electron-defect interaction $V_{im}^{\rm D}$, where m runs over the random defect sites that are located in the center of the vanadium cubes, see Fig. 3, and the *e*-*e* interaction V_{ij}. These interactions are screened by the dielectric constant ϵ_c of the core electrons and depend on the distance r through the function,

$$v(r) = \frac{e^2}{\epsilon_c\, r} \equiv V_D\, \frac{d}{r}. \tag{2.3}$$

The contribution of the t_{2g} states to the screening of the interactions is not considered in the determination of ϵ_c, but it is included explicitly in the Hamiltonian (2.1). A typical value for the core dielectric constant of the perovskite vanadates is $\epsilon_c \simeq 5$ [107]. In the following, we shall consider the potential

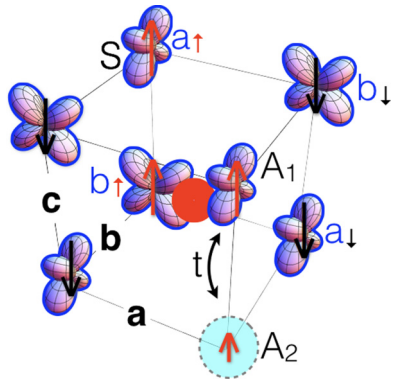

FIG. 4. Occupied vanadium t_{2g} orbitals of a V cube surrounding a Ca defect (red ball) display *G*-type orbital order with alternating $\{a,b\}$ orbitals in all three directions (the occupied c orbitals at the V ions are not shown). Spins $S = 1$ (red/black arrows) reflect *C*-type AF order and the strong Hund's coupling between $\{a,b\}$ and c electrons at V ions. Due to the kinetic energy ($\propto t$), the doped hole (blue circle) at site A_2, where the spin $s = 1/2$ of the c electron is marked, and the a electron at site A_1 strongly fluctuate on the FM *active* bond (A_1-A_2) along the c direction.

energy $V_{\rm D} \equiv e^2/\epsilon_c\, d$ as an independent parameter, instead of ϵ_c. Here, $d = (\sqrt{3}/2)a$ is the distance between the defect ion and its closest vanadium neighbors and a is the vanadium cubic lattice constant, i.e., the distance between the closest vanadium ions, see Fig. 3.

The screened interaction $v(r)$ (2.3) defines both the *e*-*e* interaction and the defect potential in case of defects with a net charge of one as in the present case, i.e.,

$$V_{im}^{\rm D} = v(r_{im}), \quad V_{ij} = \eta v(r_{ij}), \tag{2.4}$$

where r_{im} and r_{ij} represent the distances between a V ion at site i and a Ca defect at site m (r_{im}) or another V ion at site j (r_{ij}), respectively, see Fig. 4. We have introduced the parameter $\eta \in [0,1]$ in V_{ij} in Eq. (2.4) in order to explore the importance of *e*-*e* interactions and the resulting dielectric screening through the t_{2g} electrons. In the physical case $\eta = 1$, the system is charge neutral and, as a result, the negatively charged defect and the positively charged bound hole act overall as a dipole. In the case of an insulator to metal transition, the screening due to t_{2g} electrons will switch from that of a semiconductor to that of a metal, where defect charges are perfectly screened. For $\eta = 0$ instead, the monopolar potential of the negatively charged defects is unscreened as the polarization processes coming from the t_{2g} electrons (and holes) are not active.

For the t_{2g} electrons of the vanadium perovskites, the kinetic energy is defined as

$$\mathcal{H}_{\rm kin} = -t \sum_{\alpha} \sum_{\langle ij\rangle \perp \alpha} \sum_{\sigma} (d_{i\alpha\sigma}^{\dagger} d_{j\alpha\sigma} + {\rm H.c.}), \tag{2.5}$$

where we adopt a simplified notation for the t_{2g} orbital basis states [31]:

$$|a\rangle \equiv |yz\rangle, \quad |b\rangle \equiv |zx\rangle, \quad |c\rangle \equiv |xy\rangle. \tag{2.6}$$

The orbital with flavor $\alpha \in \{a,b,c\}$ lies in the plane perpendicular to the cubic crystal axis α. In order to fully understand the implications of the actual expression for the kinetic energy (2.5), one has to take into account that the hopping between

two V ions occurs along σ bonds via oxygen p orbitals. Due to the spatial symmetry of the V t_{2g} and the O p orbitals, the hopping: (i) conserves the orbital flavor α and (ii) is finite only between α orbitals along bonds $\langle ij\rangle||\gamma$ perpendicular to the direction α: $t_{ij}^{\alpha\beta} = t(1-\delta_{\alpha\gamma})\delta_{\alpha\beta}$ and $t > 0$. Thus the hopping of t_{2g} electrons is effectively 2D [43,108–110].

The most relevant Hamiltonian terms to the charge, spin, and orbital site occupations are the on-site Hubbard (U) and Hund's exchange (J_H) interactions ($\mathcal{H}_{\rm int}$) for the triply degenerate t_{2g} orbitals [111,112],

$$\begin{aligned}\mathcal{H}_{\rm int} = & U\sum_{i\alpha} n_{i\alpha\uparrow}n_{i\alpha\downarrow} - J_H\sum_{i}\sum_{\alpha\neq\beta}\mathbf{S}_{i\alpha}\cdot\mathbf{S}_{i\beta} \\ & + \frac{1}{2}\left(U-\frac{5}{2}J_H\right)\sum_{i}\sum_{\alpha\neq\beta} n_{i\alpha}n_{i\beta} \\ & + J_H\sum_{i}\sum_{\alpha\neq\beta} d^{\dagger}_{i\alpha\uparrow}d^{\dagger}_{i\alpha\downarrow}d_{i\beta\downarrow}d_{i\beta\uparrow}. \end{aligned} \tag{2.7}$$

It is the predominance of the Hubbard and of Hund's on-site interactions over the kinetic energy that establishes the Mott insulating ground state and the characteristic multiplet structure of states (see Sec. IV), which is determined by the hierarchy of the charge excitations. The multiplet structure can be considered as the fingerprint of the strong correlations characterizing these systems, and determines ultimately the magnetic properties via the spin-orbital superexchange interactions [16].

Finally, there are additional small but nevertheless relevant terms that control the spin-orbital states in these compounds, that is, they determine the anisotropy in the orbital or spin sector, respectively. The last two terms in Eq. (2.1) reflect small deviations from the cubic symmetry of the *cubic* vanadates [18,43,44], where

$$\mathcal{H}_{\rm CF} = -\Delta_c\sum_{i\sigma} n_{i\sigma c} \tag{2.8}$$

is the crystal field that splits the t_{2g} orbitals favoring the c orbital at each site ($\Delta_c > 0$) [42]. The remaining electron can then occupy either one of the degenerate a and b orbitals. The small Jahn-Teller (JT) interaction acting in the orbital space,

$$\begin{aligned}\mathcal{H}_{\rm JT} = & \frac{1}{4}V_{ab}\sum_{\langle ij\rangle\parallel ab}(n_{ia}-n_{ib})(n_{ja}-n_{jb}) \\ & - \frac{1}{4}V_c\sum_{\langle ij\rangle\parallel c}(n_{ia}-n_{ib})(n_{ja}-n_{jb}), \end{aligned} \tag{2.9}$$

favors alternating $\{a,b\}$ orbitals and AO order in the ab plane ($V_{ab} > 0$) and the *ferro* $\{a,b\}$ orbital order along the c crystal axis ($V_c > 0$) [43].

So far, the three-band t_{2g} Hamiltonian includes the interactions with charged defects, e-e interactions, i.e., short- and long-range, and it provides a faithful description of the magnetic and orbital interactions. The latter is an immediate consequence of the proper description of the atomic multiplet structure. Hence this model can describe the generic magnetic and orbital ordered phases appearing in the RVO$_3$ perovskites [50], namely two complementary spin-orbital structures: the C-AF spin with G-AO order and the G-type AF spin with C-type AO order, as well as a pure AO ordered phase [50].

In the above Hamiltonian, for the sake of simplicity and clarity of our multiband model, we have omitted certain terms. Among the neglected terms one finds: (i) the relativistic spin-orbit interaction, although small in $3d$ transition metals like vanadium, provides additional orbital fluctuations and contributes to orbital moment formation [44,66]; (ii) the orbital polarization leads to the rotation of orbitals in the proximity of defects and to flavor mixing [67,91]. Both terms influence the spin-orbital order and the metal-insulator transition, and would be relevant for a quantitative study of the phase diagram of doped vanadates, which is, however, not our intention here.

III. HARTREE-FOCK APPROXIMATION

The main aim of this paper is to analyze the evolution of the spectral weights in the PES and the IPES of strongly correlated spin-orbital system with random charged defects. This is very challenging as it is necessary to treat simultaneously and on equal footing: (i) the strong correlation problem in a multiorbital system emerging from the Hubbard interaction, the off-diagonal terms introduced by the Hund coupling and the constrained hopping – all this in presence of a strong coupling to the lattice (Jahn-Teller terms) and of strong fluctuations of all such degrees of freedom–, (ii) the local perturbations introduced by the defects into the electronic structure and the long-range nature of their Coulomb potentials, which can lead to an energy landscape that can be tuned by switching on e-e interactions from the monopolar to the dipolar regime, and (iii) the randomness of the locations of the defects that necessarily requires a statistical treatment. We shall see that the uHF approach provides an efficient calculation scheme that is able to reproduce the essence of the variations in the spectral weights of the Hubbard bands in systems with broken symmetry as the vanadates in the spin-orbital sector, which we study here.

Given the above prescriptions, the derivation of the uHF equations is standard and we do not present it here *in extenso*; more details can be found, for instance, in Refs. [86,91–93]. The essence of the derivation is that the e-e interactions are replaced by terms containing mean fields acting on the single-particle electron densities. Following this procedure, one arrives at an effective single-electron Hamiltonian,

$$\begin{aligned}\mathcal{H}_{\rm HF} = & \sum_{i\alpha\sigma}\varepsilon^{\alpha}_{i\sigma}n_{i\alpha\sigma} + \sum_{i}\sum_{\alpha\beta\sigma}\gamma^{\alpha\beta}_{i\sigma}d^{\dagger}_{i\alpha\sigma}d_{i\beta\sigma}, \\ & + \sum_{ij}\sum_{\alpha\beta\sigma}t^{\alpha\beta}_{ij}d^{\dagger}_{i\alpha\sigma}d_{j\beta\sigma}. \end{aligned} \tag{3.1}$$

This Hamiltonian can be diagonalized numerically and the mean fields appearing in the parameters (see below) and the HF states can be determined self-consistently within an iterative procedure. More details on the actual calculation scheme can be found in Appendix A, together with the treatment of the randomness in the present problem.

Following Ref. [91], we emphasize that Fock terms become active only if their off-diagonal mean fields are finite. This happens only if a single-particle term in the original Hamiltonian (a source for the specific off-diagonal mean fields) induces a finite value for them. Consequently, we adopt here only those Fock terms that couple the same orbitals at neighboring sites

(as in the kinetic energy). The terms which couple different orbitals at the same site are inactive in the present study (2.1) as such terms do not appear in the Hamiltonian Eq. (2.1) [91].

Apart from the single-particle tight-binding terms that are treated rigorously, the Hamiltonian (2.1) includes the JT terms, e-e intersite interactions $\propto V_{ij}$, and on-site terms $\propto U$ and $\propto J_H$ in Eq. (2.7). Note that the JT terms in $\mathcal{H}_{\rm JT}$ are effective density-density interactions generated by the JT distortions and, as such, they should be treated in the Hartree approximation. As these and other terms obtained in the Hartree approximation are rather straightforward to evaluate, they will not be listed here and we address below only the Fock terms. The latter terms originate from the e-e interactions $\propto V_{ij}$ and contribute effectively to the nearest-neighbor hopping terms,

$$-\sum_{\langle ij\rangle}\sum_{\alpha\sigma} V_{ij}\langle d^\dagger_{i\alpha\sigma}d_{j\alpha\sigma}\rangle(d^\dagger_{i\alpha\sigma}d_{j\alpha\sigma}+d^\dagger_{j\alpha\sigma}d_{i\alpha\sigma}). \tag{3.2}$$

Formally, such terms appear also for pairs of more distant vanadium ions, but the hopping is limited to nearest neighbors in the model Hamiltonian (2.1), so they will vanish automatically in the self-consistent solution. Finally, the on-site Coulomb interaction $H_{\rm int}$ (2.7) generates both Hartree and Fock terms, and one finds

$$\begin{aligned} &n_{i\alpha\sigma}n_{i\beta\sigma}\\ &\quad\simeq \langle n_{i\alpha\sigma}\rangle\, n_{i\beta\sigma}+n_{i\alpha\sigma}\,\langle n_{i\beta\sigma}\rangle-\langle n_{i\alpha\sigma}\rangle\,\langle n_{i\beta\sigma}\rangle\\ &\qquad-\langle d^\dagger_{i\alpha\sigma}d_{i\beta\sigma}\rangle\, d^\dagger_{i\beta\sigma}d_{i\alpha\sigma}-d^\dagger_{i\alpha\sigma}d_{i\beta\sigma}\,\langle d^\dagger_{i\beta\sigma}d_{i\alpha\sigma}\rangle\\ &\qquad+\langle d^\dagger_{i\alpha\sigma}d_{i\beta\sigma}\rangle\,\langle d^\dagger_{i\beta\sigma}d_{i\alpha\sigma}\rangle, \end{aligned} \tag{3.3}$$

$$\begin{aligned} &S^+_{i\alpha}S^-_{i\beta}\\ &\quad= d^\dagger_{i\alpha\uparrow}d_{i\alpha\downarrow}d^\dagger_{i\beta\downarrow}d_{i\beta\uparrow}\\ &\quad\simeq -\langle d^\dagger_{i\alpha\uparrow}d_{i\beta\uparrow}\rangle\, d^\dagger_{i\beta\downarrow}d_{i\alpha\downarrow}-d^\dagger_{i\alpha\uparrow}d_{i\beta\uparrow}\,\langle d^\dagger_{i\beta\downarrow}d_{i\alpha\downarrow}\rangle\\ &\qquad+\langle d^\dagger_{i\alpha\uparrow}d_{i\beta\uparrow}\rangle\,\langle d^\dagger_{i\beta\downarrow}d_{i\alpha\downarrow}\rangle, \end{aligned} \tag{3.4}$$

$$\begin{aligned} &d^\dagger_{i\alpha\uparrow}d^\dagger_{i\alpha\downarrow}d_{i\beta\downarrow}d_{i\beta\uparrow}\\ &\quad\simeq \langle d^\dagger_{i\alpha\uparrow}d_{i\beta\uparrow}\rangle\, d^\dagger_{i\alpha\downarrow}d_{i\beta\downarrow}+d^\dagger_{i\alpha\uparrow}d_{i\beta\uparrow}\,\langle d^\dagger_{i\alpha\downarrow}d_{i\beta\downarrow}\rangle\\ &\qquad-\langle d^\dagger_{i\alpha\uparrow}d_{i\beta\uparrow}\rangle\,\langle d^\dagger_{i\alpha\downarrow}d_{i\beta\downarrow}\rangle. \end{aligned} \tag{3.5}$$

Note, however, that these latter Fock terms, mixing the orbitals, are included here only to exhaust the approximate treatment of $H_{\rm int}$ (2.7). They would be active, for instance, if the orbitals were optimized locally by a finite orbital polarization interaction [91], that is not considered here though. Therefore we do not include them in our analysis as it suffices to decouple the individual terms in Eq. (2.7) using Hartree approximation.

The uHF calculations in this work are performed for three different sets $\{A,B,C\}$ of fundamental interaction parameters U, J_H and V_D listed in Table I for convenience. They have been motivated by different experimental results and/or considerations as parameters relevant for RVO$_3$. Set A is deduced in this work from PES data for the undoped LaVO$_3$ compound [70] and gives the positions of the LHB and the UHB multiplet structure in qualitative agreement with the PES and IPES spectra of Maiti and Sarma [70], see Fig. 2. Set B was deduced from the optical spectroscopy and the magnetic properties of YVO$_3$ [106] and was used before to (i) analyze the magnetic transition from G-AF to C-AF phase in YVO$_3$ [67], and (ii) study the defects in Y$_{1-x}$Ca$_x$VO$_3$ [63,91]. Set C is dictated by a simplified analysis of the PES and IPES data in Ref. [69], as explained in more detail in Sec. IV B. If not stated differently, we consider $\eta = 1$ in Eq. (2.4) and vary the doping in the range $x \in (0,0.5]$.

TABLE I. The three parameter sets for the interactions in Hamiltonian (2.1) used in the numerical uHF calculations; all parameters are given in eV. The set A refers to LaVO$_3$ and was used to obtain the theoretical spectrum in Fig. 2; the remaining sets are for doped systems and include a finite defect potential $V_{\rm D}$ (2.3).

Set	Δ_c	U	J_H	V_{ab}	V_c	$V_{\rm D}$
A	0.1	4.1	0.45	0.03	0.05	—
B	0.1	4.0	0.6	0.03	0.05	1.0
C	0.1	4.5	0.5	0.03	0.05	2.0

Sets A and C are rather similar concerning the most important feature, namely the distance of the centers of LHB and UHB given by $(U-3J_H) = 2.75$ and 3.0 eV, respectively. Set B instead was determined from a model Hamiltonian with only local Hubbard-Hund type interactions, the missing excitonic corrections [113,114] to the optical gap require in this case a significantly smaller value $(U-3J_H) = 2.2$ eV. An analysis of the parameter V_D that defines the defect potential strength as well as the e-e interaction will be given in Sec. VIII. Although our work focuses on the role played by e-e interactions, we present in the following calculations both for the *realistic* set C and for the set B, because set B displays features that are somewhat hidden in the spectra calculated using set C.

IV. DOPING DEPENDENCE OF THE DENSITY OF STATES

A. Multiplet structure and sum rules

In this section, we begin our study of the doped Mott insulator with the DOS $N(\omega)$ of the multiband model in the phase with C-type spin and G-type orbital order (i.e., C-AF/G-AO phase). Within the uHF method, $N(\omega)$ describes processes that correspond to the addition of an electron for $\omega > \mu$ and to the removal of an electron for $\omega < \mu$, where μ is the chemical potential. Thus $N(\omega)$ provides information relevant for the interpretation of PES and IPES or tunneling experiments [104,105]. The numerical results presented in this paper are obtained for a cluster of $N_a = 8\times 8\times 8$ vanadium ions with periodic boundary conditions, after averaging over $M = 100$ randomly chosen different Ca defect *realizations* $\{s\}$ (i.e., sets of randomly chosen Ca defect locations) at a given doping $x \in (0,0.5]$. We use as standard parameters set B of Table I and $t = 0.2$ eV [43]. For each defect realization s, we determine the $6\times N_a$ eigenvalues $\{\epsilon_{s,l}\}$ and the value of the Fermi energy μ_s. Next, we calculate the final averaged DOS $N(\omega)$, representative for the whole system with N_a sites and xN_a randomly distributed defects, as an average over the M defect realizations,

$$N(\omega) \equiv \frac{1}{M}\sum_{s=1}^{M}\left[\frac{1}{N_a}\sum_{l=1}^{6N_a}\delta(\omega+\mu_s-\epsilon_{s,l})\right]. \tag{4.1}$$

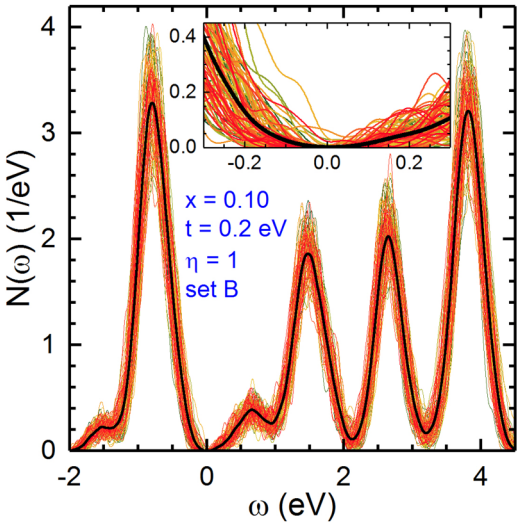

FIG. 5. Statistical average of t_{2g} DOS $N(\omega)$ (4.1) (thick solid black line) as obtained from $M = 100$ random defect realizations (thin solid green-to-red lines) for $t = 0.2$ eV and including e-e interactions ($\eta = 1$) at doping concentration $x = 0.1$. Other parameters as in set B of Table I. Inset shows the zoom of the DOS near the Fermi energy at $\omega = 0$.

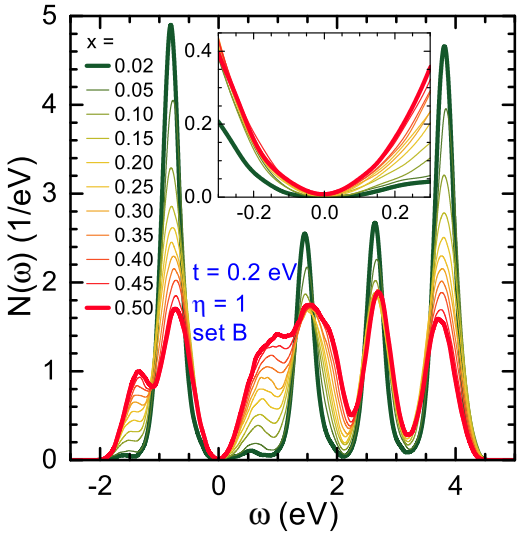

FIG. 6. Doping dependence of t_{2g} DOS $N(\omega)$ (4.1) as obtained from $M = 100$ random defect realizations for $t = 0.2$ eV and including e-e interactions ($\eta = 1$) for increasing doping $x \in [0.02,0.50]$. Other parameters as in set B of Table I. Inset shows the zoom of the DOS near the Fermi energy at $\omega = 0$.

The shapes of the structures arising in the LHB and the UHB are somewhat different in each of the defect realizations s, but all of them show the characteristic maxima to be discussed below, see Fig. 5.

Each charged defect adds a hole to the system, thus the averaging over the different defect realizations is performed for an electron density $n = N_0/N_a = 2 - x$ per V ion, and the chemical potential is determined as $\mu_s = (\epsilon_{s,N_0} + \epsilon_{s,N_0+1})/2$. The obtained DOS satisfies the sum rule:

$$\int_{-\infty}^{\infty} d\omega\, N(\omega) = 6, \tag{4.2}$$

and determines the total number of t_{2g} electrons per site,

$$\int_{-\infty}^{0} d\omega\, N(\omega) = n, \tag{4.3}$$

where the overall chemical potential is at $\omega = 0$. To control the gradual change of the spectral weights found for the particular structures observed in the DOS, it is convenient to introduce the integrated DOS $n(\omega)$ defined as follows:

$$n(\omega) \equiv \int_{-\infty}^{\omega} d\omega'\, N(\omega'). \tag{4.4}$$

Undoped YVO_3 (or $LaVO_3$) is a Mott insulator and its DOS consists of a LHB and a UHB, separated by a wide MH gap, shown in Fig. 6. The reference here are the data obtained at the lowest value of doping $x = 0.02$. The LHB is given by a single maximum with total spectral weight $w_{\rm LHB} = 2$ in the undoped system, which corresponds to possible one-electron excitations in the PES, see Fig. 2. In contrast, the UHB has three distinct maxima, which reflect the multiplet structure of the excitations accessible in the IPES for the undoped system, as discussed for the two-flavor model in Ref. [67]. We observe that the full width W (at half maximum) of all these structures and of the LHB is $W \simeq 0.5$ eV at low and moderate doping. One could argue that this broadening originates from the incoherence expected for hole (electron) polaron motion in a system with broken symmetry. However, one would expect for a free polaron a width $W_{\rm inc} = 4\sqrt{z-1}\,t$ [115], where the number of neighbors for the effective 2D hopping of t_{2g} electrons is $z = 4$. This would suggest a much larger value $W_{\rm inc} \approx 1.4$ eV. We take this as an indication that the doped holes or polarons are immobile and bound to defects. Hence the broadening is predominantly due to the distribution of the local energies due to the random defect potentials (see Sec. IV D). We have shown before that the width of the LHB is ~1.0 eV in the absence of e-e interactions, and is *reduced* to ~0.5 eV in the presence of long-range Coulomb interactions [63], due to the screening of the defect potentials resulting from t_{2g} electrons.

A particularly exciting feature is the persistence of a soft gap right at the chemical potential $\omega = 0$ in Fig. 6. Although many defect states fill into the MH gap with increasing doping x, it appears that there is a mechanism at work resulting in the highest occupied states and the lowest unoccupied states repelling each other. This is reminiscent of the Peierls effect, but also of the Coulomb gap mechanism. The detailed analysis of the origin of the DS gap in our model is a central issue in this and the following sections.

The DOS obtained for doped $R_{1-x}Ca_xVO_3$ systems preserves the main features seen at $x = 0$: the LHB and the UHB are separated by the MH gap, see Fig. 6. With increasing doping $x > 0$, the spectral weights below (above) the Fermi energy change in a systematic way. In particular, the fundamental splitting of the MH gap ($U - 3J_H$) persists up to surprisingly high doping. There arise also new features due to defect states with intensities growing with doping x—one finds a second structure in the LHB at low energy, see Fig. 6. A similar structure with a faster increase of the spectral weight as a function of doping x is observed inside the MH gap at the low-energy edge of the first maximum in the UHB. At the same

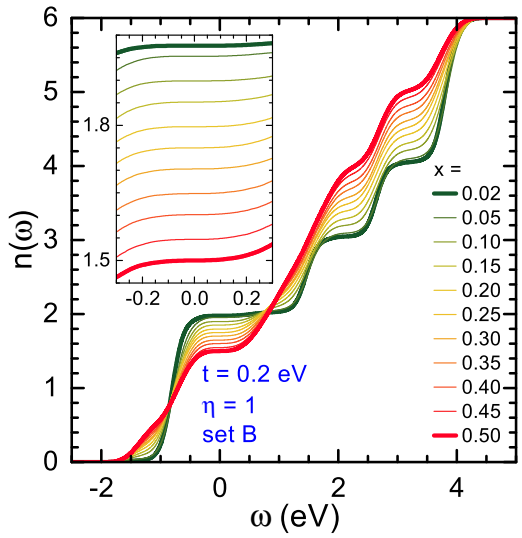

FIG. 7. Integrated density of states $n(\omega)$ (4.4) for different doping concentration $x \in [0.02,0.50]$ obtained for the spectra presented in Fig. 6 for $t = 0.2$ eV and including e-e interactions ($\eta = 1$). Other parameters as in set B of Table I. Inset shows the zoom of the $n(\omega)$ near the Fermi energy at $\omega = 0$.

time, the Hubbard subbands found at $x = 0$ persist, but show decreasing spectral intensities with increasing x. We analyze these changes in the next section.

It is insightful to analyze the evolution of the spectra in Fig. 6 by considering the integrated DOS $n(\omega)$ (4.4). At small doping $x = 0.02$, $n(\omega)$ is characterized by several steps that reflect the wide MH gap (wide plateau around $\omega = 0$) and the minima of $N(\omega)$ that separate three different states in the UHB (two narrow plateaus), see Fig. 7. With increasing x, the plateaus shrink due to the appearance of more and more defect states inside the different gaps. The DOS integrated up to the Fermi energy $\omega = 0$ gives the total electron density, $n(0) = n$. That is, the weight of the LHB including the low energy satellite of the LHB is $(2 - x)$. A minute increase just above $\omega = 0$ indicates that the MH gap is accompanied by a small maximum, arising at finite doping, just above the Fermi energy. For increasing x, the maximum above the Fermi energy extends over a broader range, $0.2 < \omega < 2.0$, suggesting that all structures arising at finite doping are all absorbed within this broader and broader maximum. We turn back to this discussion below in Sec. IV D.

B. Atomic limit: Exact solution

It is convenient to recall first the main features of the one-particle spectra for the nondegenerate Hubbard model. One of its main successes was to elucidate the variation of the electronic structure in a strongly correlated electronic system with increasing/decreasing electron density and to provide its explanation. It captures the evolution of spectral weights within the individual Hubbard bands [116–122]. Indeed, in a Mott insulator described by the nondegenerate Hubbard model, the DOS consists of two Hubbard bands, the LHB and the UHB, with equal spectral weights at half filling. These weights, however, change rather fast in a hole-doped insulator when the number of unoccupied states at energies just above the Fermi energy increases—these states belong to the LHB in a system without charged defects [116–119]. A similar behavior is found for electron doping by applying the particle-hole symmetry. The evolution of spectral weights with increasing doping has been explained within a systematic expansion in (t/U) in the Hubbard model [121], but frequently it is sufficient to use only the leading terms of this expansion, which stem from the atomic limit and are written in terms of the electron density. For the nondegenerate Hubbard model at hole doping x this approximation predicts that the LHB has altogether $(1 + x)$ states, with $(1 - x)$ states below and $2x$ (unoccupied) states above the Fermi energy. Below, we generalize this result to a degenerate Hubbard model following the early ideas on this subject [123] and more recent treatment of the doped perovskite vanadates, where it was demonstrated that the excitations that contribute to the UHB correspond to the multiplet structure of V^{2+} ions [67].

In the following, we adopt the atomic perspective and analyze the C-AF/G-AO states with broken symmetry, addressing also possible deviations resulting from the finite kinetic energy $\propto t$ and from the uHF. For a vanadium perovskite with charged defects the holes added to vanadium ions generate local t_{2g}^1 configurations with probability x, while the t_{2g}^2 states occur with probability $(1 - x)$ in a doped system. This is schematically represented by the ground state wave function $|\Phi\rangle$ for a vanadium ion in Fig. 8(a). In the case depicted in Fig. 8 doping has removed an $|a\uparrow\rangle$ electron which has a higher energy than the $|c\uparrow\rangle$ electron due to the small crystal field $\Delta_c = 0.1$ eV, see also Fig. 4. We start from these states to explain the possible PES and IPES excitations, that result from electron removal and addition processes, and lead to final states in the LHB and the UHB, respectively, but also to various defect states.

In IPES, one electron is added in the $d^n \to d^{n+1}$ process, either to the $|c\uparrow a\uparrow\rangle$ initial configuration of V^{3+} ion ($n = 2$), see Fig. 8(b), or at a V^{4+} ion ($n = 1$), with a hole in place of $|a\uparrow\rangle$ electron initial state, see Fig. 8(c). As the doped sites are typically direct neighbors of a charged defects, the electron energies at these sites are increased by V_D (2.3). Thus the HS states generated by $d^1 \to d^2$ IPES transitions appear as in-gap states above the Fermi energy. Thereby, the multiplet structure of d^2 final states overlaps partially with the t_{2g}^3 multiplet states of the UHB as can be inferred from Fig. 8. Altogether, the states excited in IPES are quite numerous, four and five for the two cases listed above, and their zth spin component S^z is either increased by $1/2$ or decreased by $1/2$. The exact energies of the atomic $S = 3/2$ ($S = 1$) HS and $S = 1/2$ ($S = 0$) LS states accessible in the IPES excitations at vanadium ions in d^2 (d^1) configurations are given in Table II and compared with the energies found in the uHF approximation.

Taking all the states generated in IPES one finds their total weight of $(4 + x)$, which is a generalization of the $(1 + x)$ found in the nondegenerate Hubbard model [117] and the $(3 + x)$ for the two-flavor model in Ref. [67]. The UHB obtained for $d^2 \to d^3$ excitations has three subbands corresponding to the atomic multiplet structure with energies $(U - 3J_H)$, U, and $(U + 2J_H)$ as given in Table II. They are found from the exact solution treating rigorously the Coulomb interactions for t_{2g}^3 excited states in the atomic limit. In a doped system, the initial t_{2g}^2 state occurs in the wave function $|\Phi\rangle$ with the probability $(1 - x)$, see Fig. 8(a). Therefore the weights

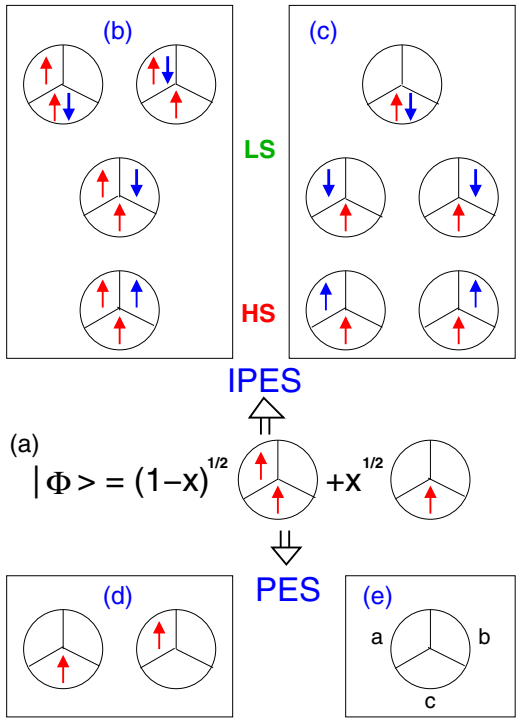

FIG. 8. Artist's view of possible PES (electron removal, bottom) and IPES (electron addition, top) excitations in doped $R_{1-x}Ca_xVO_3$ compounds, as obtained in the HF approximation. In (a), we show a representative (on the ↑-spin sublattice) ground state $|\Phi\rangle$ with electron spins shown by red arrows—it includes both $|c{\uparrow}a{\uparrow}\rangle$ and $|c{\uparrow}\rangle$ local states in a doped system with amplitudes $\sqrt{1-x}$ and $\sqrt{x}$. Adding an electron in IPES (UHB) (blue arrows) generates in this ground state either: (b) four possible t_{2g}^3 final states with probabilities $(1-x)$ each or (c) five possible t_{2g}^2 final states with probabilities x each (with some modifications, see the main text). The states excited in IPES are either HS or LS, with their energies listed in Table II. Removing an electron (replacing an arrow by a hole) in PES reduces the spin by 1/2 and gives (d) either the two t_{2g}^1 excited states with probabilities $(1-x)$ in the LHB, or (e) an empty t_{2g}^0 final state with probability x. In each panel, three t_{2g} orbitals are labeled as $\{a,b,c\}$ (2.6), with the convention shown in (e).

of these excitations are: $(1-x)$, $2(1-x)$, and $(1-x)$. This weight distribution is modified when quantum fluctuations are neglected, see below.

Let us compare first the results obtained for the PES and IPES spectra with the experimental results for undoped $LaVO_3$ shown in Fig. 2. The spectrum consists of two distinct structures, the LHB and the UHB separated by a broad MH gap. From the experimental spectra, one learns that the distance that separates the LHB and the HS excitation in the UHB is 3.0 eV. This gives the first experimental constraint on the on-site Coulomb interaction parameters $\{U, J_H\}$—this energy difference obtained in the theory is $(U-3J_H)$, see Table II. Furthermore, for the undoped $LaVO_3$, the HF theory predicts three peaks in the UHB, with the HF energies of $(U-3J_H)$, $(U-J_H)$, and $(U+J_H)$ for the HS, LS_1, and LS_2 excitations, see Table II. The energetic separation of the LS_2 and the HS states is thus $4J_H$ that determines the lower bound for the width of the UHB. Note that the same result would be

TABLE II. Spectral weights w_n and atomic excitation energies ε_n in IPES and PES processes available in doped $R_{1-x}Ca_xVO_3$, leading to final state configurations shown in Fig. 8, as found in the uHF approximation (HF). The energies that involve a doped ion (d^1) "close to a defect" are increased by the energy V_D. The energies found in uHF (HF) are compared with those of a free ion (exact), where quantum fluctuations are also included. The HF approach reproduces exact energies of a free ion for PES and for HS IPES states, where only a single energy is shown. For convenience, the PES excitation energy for the host is taken as a reference, $\varepsilon_{LHB}=0$ (here, the small crystal-field splitting Δ_c is ignored).

				ε_n	
IPES	Final state	Spin	w_n	HF	Exact
$d^2\to d^3$	$\lvert c{\uparrow}a{\uparrow}b{\uparrow}\rangle$	HS	$1-x$	$U-3J_H$	
	$\lvert c{\uparrow}a{\uparrow}b{\downarrow}\rangle$	LS	$1-x$	$U-J_H$	U
	$\lvert c{\uparrow}a{\uparrow}c{\downarrow}\rangle$	LS	$1-x$	$U+J_H$	U
	$\lvert c{\uparrow}a{\uparrow}a{\downarrow}\rangle$	LS	$1-x$	$U+J_H$	$U+2J_H$
$d^1\to d^2$	$\lvert c{\uparrow}a{\uparrow}\rangle$	HS	x	V_D	
	$\lvert c{\uparrow}b{\uparrow}\rangle$	HS	x	V_D	
	$\lvert c{\uparrow}b{\downarrow}\rangle$	LS	x	V_D+J_H	V_D+2J_H
	$\lvert c{\uparrow}a{\downarrow}\rangle$	LS	x	V_D+J_H	V_D+2J_H
	$\lvert c{\uparrow}c{\downarrow}\rangle$	LS	x	V_D+3J_H	V_D+5J_H
PES	Final state	-	w_n	ε_n	
$d^2\to d^1$	$\lvert c{\uparrow}\rangle$	-	$1-x$	0	
	$\lvert a{\uparrow}\rangle$	-	$1-x$	0	
$d^1\to d^0$	$\lvert 0\rangle$	-	x	$V_D-(U-3J_H)$	

obtained in the electronic structure calculations implementing the leading part of local Coulomb interactions [124]. The overall width of the UHB is expected to be enhanced by the quantum fluctuations beyond the uHF by $\sim J_H$ and by the experimental broadening.

As explained above, the highest excitation energy for the LS_2 states is doubly degenerate in HF, which gives here twice larger spectral weight than that of the other two excitations, HS and LS_1. In contrast, the LS_1 state is doubly degenerate when quantum effects are included (see Table II) and the correct weight distribution is 1:2:1 for the HS, LS_1, and LS_2 states. In Fig. 2, we have adjusted the spectral weights of the uHF spectra accordingly to achieve a better agreement with experiment. Unfortunately, the individual excitations within the UHB cannot be resolved in the data [70]. The whole spectrum formed by the LHB and UHB is reproduced well by the theory, see Fig. 2, after adjusting the two characteristic parameters $\{U, J_H\}$ that define the position of the maximum seen in the UHB at the energy $(U-J_H)$ of the LS_1 state, i.e., relative to the energy of the LHB. The best fit was obtained with $U=4.1$ eV and $J_H=0.45$ eV that defines the set A of Table I. Apart from a somewhat decreasing overall experimental spectral weight with increasing excitation energy ω, which cannot be reproduced without additional information about the matrix elements, the agreement between the experiment and the theory predictions is indeed very satisfactory and suggests the presence of a multiplet structure within the UHB.

The analysis of the IPES excitations summarized in Table II elucidates additional features generated in the spectra by doping. For the $|c{\uparrow}\rangle$ component of the ground-state wave

function $|\Phi\rangle$ [Fig. 8(a)], with a hole in the initially occupied a orbital, two HS states and three LS states may be generated by IPES, see Fig. 8(c). Each of these states will have a spectral weight x. In contrast to the excitations occurring in the host shown in Fig. 8(b), the HS excitations at a doped site include two final t_{2g}^2 states, either $|c\uparrow a\uparrow\rangle$ or $|c\uparrow b\uparrow\rangle$, with the same local Coulomb energy $(U-3J_H)$ as for t_{2g}^2 host states. Thus these excitation energies ε_n do not include the intraatomic Coulomb U or exchange J_H and would appear just above the LHB in the absence of a defect potential (i.e., at $V_{\rm D}=0$) [117]. However, in reality the $d^1\to d^2$ excitation energy is enhanced by large $V_{\rm D}$ near the charged impurity in the center of the cube occupied by the defect (Fig. 4) and these unoccupied states appear deep within the MH gap. The defect potential $V_{\rm D}$ acts on any local state and enhances its excitation energy, see Table II. The two LS states with two different orbitals singly occupied have the final energies of $(U-J_H)$, so the excitation energies are $2J_H$. The excitation involving double occupancy $|c\uparrow c\downarrow\rangle$ is more subtle. This state itself is not an eigenstate of $H_{\rm int}$ (2.7) as a double occupancy couples by the term $\propto J_H$ to $|a\uparrow a\downarrow\rangle$ or $|b\uparrow b\downarrow\rangle$ state. As a result, the highest excitation energy $(V_{\rm D}+5J_H)$ is obtained only for one (fully symmetric with respect to orbital permutations) eigenstate while the energy $(V_{\rm D}+2J_H)$ for the other two. Eventually, the configuration $|c\uparrow c\downarrow\rangle$ shown in Fig. 8(c) is found with the probability of $1/3$ in each of these eigenstates. Hence, by performing the corresponding projections, one finds that the final exact atomic spectral weights for the energies $(V_{\rm D}+2J_H)$ and $(V_{\rm D}+5J_H)$ are $8x/3$ and $x/3$.

Here again quantum fluctuations contribute and the HF energies of two interorbital LS states, $|c\uparrow a\downarrow\rangle$ and $|c\uparrow b\downarrow\rangle$, are lower by J_H, i.e., by the same amount as found for the final LS states in the case of $d^2\to d^3$ excitations. The other states are given by the double occupancies that are here eigenstates at energy U, so the excitation energy for the accessible $|c\uparrow c\downarrow\rangle$ state is $(V_{\rm D}+3J_H)$, see Table II. The HF spectral weights for the LS_1 and LS_2 states are thus $2x$ and x.

The PES excitations are much simpler than the IPES ones as just one electron is removed from either component of the ground state wave function shown in Fig. 8(a) and the spin is then reduced by $1/2$. The $d^2\to d^1$ excitations in the host have approximately the same excitation energy taken here as the reference, $\varepsilon_n=\varepsilon_{\rm LHB}=0$ (we neglect again the crystal-field term $\propto\Delta_c$). In contrast, a PES excitation at the hole site, $d^1\to d^0$, starts from the $|c\uparrow\rangle$ state, so the energy of the d^2 reference configuration is subtracted from $V_{\rm D}$ in Table II.

C. Spectral weight distribution in the atomic limit

To illustrate the above theory, we determined the individual structures in PES/IPES spectra and their evolution with increasing doping $x\in[0.02,0.50]$ for $t=0.01$ eV. Here, the kinetic energy is chosen to be very small indeed to generate the results representative for the atomic limit. In Fig. 9, one observes that the MH gap persists in doped systems. The LHB is well separated from the HS excitation in the UHB by the MH gap for the entire doping regime. The states arising within the MH gap do not close this gap, but develop a novel kinetic gap analyzed in more detail in the next Sec. V.

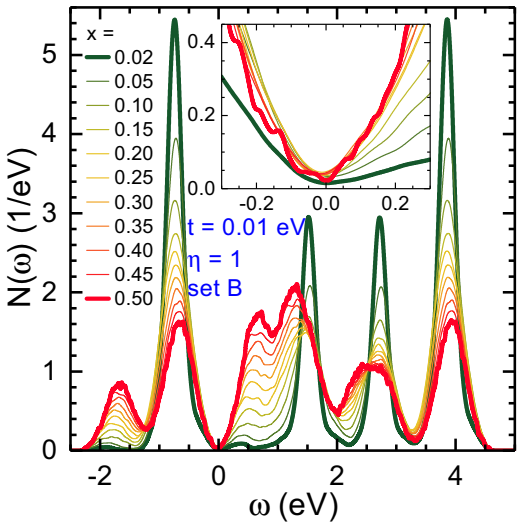

FIG. 9. Doping dependence of t_{2g} DOS $N(\omega)$ (4.1) as obtained from $M=100$ random defect realizations for $t=0.01$ eV and including e-e interactions ($\eta=1$) for increasing doping $x\in[0.02,0.50]$. Other parameters as in set B in Table I. Inset shows the zoom of the DOS near the Fermi energy at $\omega=0$.

PES excitations (at $\omega<0$) are seen in the spectra as two structures: (i) the LHB corresponding to individual $d^2\to d^1$ transitions at V sites that are not nearest neighbors of defects; (ii) a satellite below the LHB at energy ~-2.0 eV, i.e., originating from $d^1\to d^0$ processes at sites occupied by doped holes, see Fig. 9. When the doping x increases, the spectral weight of the PES part is altogether $\sim(2-x)$, which consists of the main peak representing the LHB $\sim(2-2x)$ and a satellite generated by the excitations at the hole sites with growing spectral weight $\sim x$. This agrees with the spectral weights of the PES states listed in Table II. The satellite moves gradually towards the LHB, reaching energy ~-1.7 eV at $x=0.45$. Excitations from undoped sites near defects are close to the Fermi energy and can be well resolved from the main maximum in the LHB.

The three multiplet transitions $d^2\to d^3$ that appear in the IPES part of the uHF spectra are surprisingly well resolved even at high doping. The spectral weights of these UHB states of the host compound are $(1-x)$, $(1-x)$, and $2(1-x)$ for the HS, LS_1 and LS_2 states, see Fig. 9. The defect related features in the IPES part ($\omega>0$) due to $d^1\to d^2$ excitations are better resolved here than in case of $t=0.2$ eV (Fig. 6). There are two distinct peaks that grow with doping within the MH gap, at energies ~0.6 and ~1.2 eV. While the weight of the lower maximum accumulates the weight $\sim2x$, the weight if the second maximum appears even somewhat larger. We recall that the weight of the satellite below the LHB is $\sim x$, see Table II. The third maximum induced by doping falls near the minimum separating the HS from the LS_1 excitation in the reference multiplet structure of the UHB (for these parameters) and has a lower weight $\sim x$. In addition, a spectacular evolution of pseudogap in $N(\omega)$ close to $\omega=0$ is found (see inset). The highly asymmetric spectrum changes gradually to an almost symmetric one with increasing x.

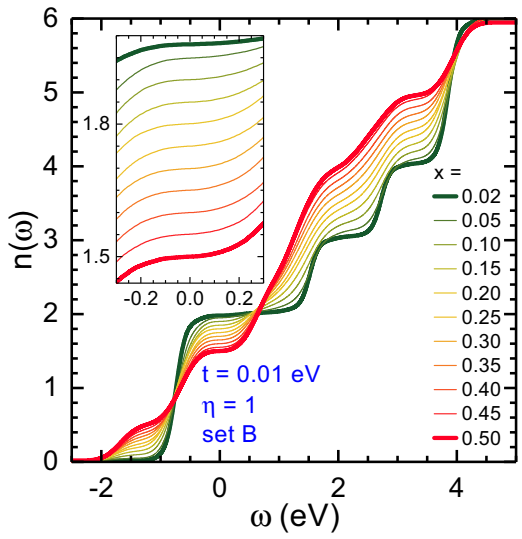

FIG. 10. Integrated density of states $n(\omega)$ (4.4) for different doping $x \in [0.02, 0.50]$ obtained for the spectra presented in Fig. 9 at $t = 0.01$ eV and including e-e interactions ($\eta = 1$). Other parameters as in set B in Table I. Inset shows the zoom of the $n(\omega)$ near the Fermi energy at $\omega = 0$.

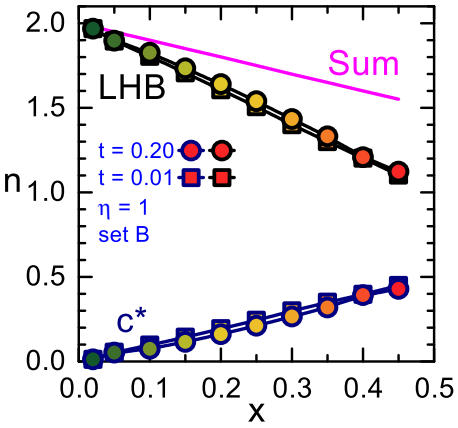

FIG. 11. Doping dependence of the total spectral weight below the Fermi energy (sum, magenta line), of the LHB (LHB, black symbols) originating from undoped V sites and the satellite c^* (blue symbols) due to $d^1 \rightarrow d^0$ PES annihilation processes of occupied c orbitals at V ions in d^1 states. Data is obtained near the atomic limit for $t = 0.01$ eV (squares) and at the value $t = 0.2$ eV realistic for $Y_{1-x}Ca_xVO_3$ (circles). Other parameters as in set B in Table I.

The modifications of the DOS $N(\omega)$ with increasing doping x shown in Fig. 9 can be even better appreciated by analyzing the integrated DOS, see Fig. 10. First of all, one finds an almost flat plateau in the integrated DOS at $n(\omega) \simeq 1.98$ at low doping $x = 0.02$, and the plateau at $\omega = 0$ persists at higher doping. At $x = 0.02$, large steps of $(1 - x)$ are found for the energies of the HS and LS_1 states in the UHB, and of $2(1 - x)$ at energy of the LS_2 state. Note that this latter excitation is well separated from the structures generated by excitations at sites doped by holes as the former energies are lower. Most importantly, the excitation energies are constant and are not influenced by increasing doping, reflecting the robust local character of both $d^2 \rightarrow d^3$ and $d^1 \rightarrow d^2$ processes.

At the lowest doping $x = 0.02$, one is sufficiently close to the reference undoped system characterized by the LHB at $\omega \sim -0.8$ eV, and the weak satellite feature with low intensity arises at $\omega \simeq -2.0$ eV, identified by finite $n(\omega)$ for $-2.0 < \omega < -1.0$ eV. By removing a single electron one gains here the energy V_D as this electron before the removal feels the potential of the charged defect V_D in the center of the cube, see Table II. Indeed, this latter excitation energy is lower than that at the center of the LHB, as observed in Fig. 9. Faster increase of $n(\omega)$ follows close to $\omega = -0.8$ eV and afterwards the integrated weight grows again very slowly. Finally, the spectral features that grow with increasing doping in Fig. 9 are responsible for the dramatic deformation of a distinct step structure seen in Fig. 10 at $x = 0.02$ towards an almost steady increase of $n(\omega)$ from the onset of the LHB to the top of the UHB, except for a quite narrow plateau near the Fermi energy shown in the inset.

We also observe a remarkable feature in Fig. 10. Independently of actual doping x, the integrated DOS reaches the value of two electrons per site at $\omega \simeq 0.7$ eV. This shows that the spectral weight missing in the PES part is compensated by the HS $d^1 \rightarrow d^2$ excitations which have an approximately constant energy above the Fermi level in the entire doping regime. A similar point is found at $\omega \simeq -0.8$ eV and the filling of $n(\omega) = 0.8$—here it falls around the maximum of the LHB. These points are quite reminiscent of the isosbestic point found in the specific heat of correlated systems [125,126]. Here the two isosbestic points originate from the doping dependent spectral weight transfers between the host Hubbard bands and the defect states, that correspond to the final states of the $d^1 \rightarrow d^0$ and $d^1 \rightarrow d^2$ transitions, respectively.

Summarizing, by analyzing the data in Figs. 6 and 9, one concludes that the spectral weights found in the numerical calculations both confirm those found in the atomic limit, see Table II. The total spectral weight of the occupied part of the DOS, $2 - x$, reproduces the average electron density below the Fermi energy. This weight consists of that of the LHB, represented by the main peak in the spectra, which corresponds to $d^2 \rightarrow d^1$ transitions at undoped sites with the total intensity $2(1 - x)$, and that of the satellite growing at low energy with the weight of x as it reflects the $d^1 \rightarrow d^0$ excitations at the V ions with doped holes in bound states near the defects. The predicted linear behavior $\propto x$ is indeed reproduced at $t = 0.01$ eV, see Fig. 11, while only a small deviation from it is observed for $t = 0.2$ eV. One finds that the spectral weight in the LHB is somewhat enhanced at the expense of the $d^1 \rightarrow d^0$ satellite. This behavior is reminiscent of the kinetic spectral weight transfer in the nondegenerate Hubbard model [116,117].

D. Active bond and satellite of the LHB

We emphasize that the satellite structure arising from the $d^1 \rightarrow d^0$ excitation is well separated from the remaining states in the LHB only in a particular range of parameters and in addition when the hopping is small, $t = 0.01$ eV. For such an immobile hole the excitation energy is practically the same as in the atomic limit, see Table II,

$$E_m^{(0)} = E_{\mathrm{LHB}} + V_D - (U - 3J_H). \tag{4.5}$$

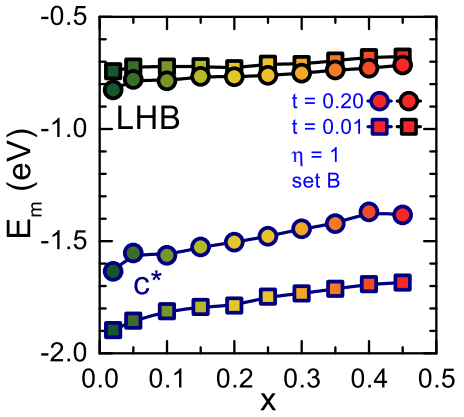

FIG. 12. Excitation energies E_m assigned to the LHB $d^2 \to d^1$ excitations and to the satellite c^* attributed to $d^1 \to d^0$ excitations arising from holelike small polarons, where the doped holes (or d^1 configurations) are localized at V-ions close to a charged Ca defect. Data are shown for $t = 0.2$ eV (circles) and for the atomic limit $t = 0.01$ eV (squares). Other parameters as in set B of Table I.

Thus, to get the excitation energies in the case of $t = 0.01$ eV one has to include the energy corresponding to the center of the LHB, being $E_{\rm LHB} = -0.7$ eV in Fig. 12, and combine it with the energy of the $d^1 \to d^0$ excitation $(V_{\rm D} - U + 3J_H)$, and one arrives at the excitation energy $E_m^{(0)} = -1.9$ eV shown in Fig. 12 for the low doping $x = 0.02$.

Consider now a doped site i at finite and increasing t. The hole as well as the other occupied V neighbors closest to a given Ca^{2+} defect (on a cube $\mathcal{C}_m$ surrounding a defect at site m) feel the potential $V_{\rm D}$ [91]. The hole delocalizes partly along the active FM bond $\langle ij\rangle \| c$ axis, and electronic configurations at sites i and j change from $(b\uparrow)^0$ and $(b\uparrow)^1$ to $(b\uparrow)^\delta$ and $(b\uparrow)^{1-\delta}$ [with $\delta < 0.5$ and $(c\uparrow)^1$ electron at each site]. This results in the modification of excitation energies at both sites and one finds instead of Eq. (4.5):

$$E_m^{(i)} = E_{\rm LHB} + V_{\rm D} - (U - 3J_H)(1-\delta), \qquad (4.6)$$

$$E_m^{(j)} = E_{\rm LHB} + V_{\rm D} - (U - 3J_H)\,\delta. \qquad (4.7)$$

This is illustrated through a calculation for well annealed, or equivalently short-range-potential random, charged defects in Fig. 13. In this figure, together with the reference overall multiplet structure (panel a), the partial DOS $N_{i\gamma\sigma}(\omega)$ at three V sites of the defect cube (see Fig. 4) are displayed. Namely, sites A_1 (panel b) and A_2 (panel c) that belong to the FM active bond that basically accommodates the doped hole, and, for comparison, at a site with two electrons which we call a spectator (S) site, see Fig. 4(d). In the latter case, both electrons a and c feel the Hubbard interaction $(U - 3J_H)$. The remaining single a electron on the active bond forms a bonding state, whose polarity is determined by several factors: (i) the interplay of kinetic energy and JT-fields and (ii) in the long-range-potential case with random defects, the random fields of the other defects. Even in absence of random defect potentials a hole distribution polarized along the c axis is expected, favored by the JT potentials in the symmetry broken G-AO state.

The energies of the occupied c levels at sites A_1 and A_2 in Fig. 13 are very different, as they are controlled by the

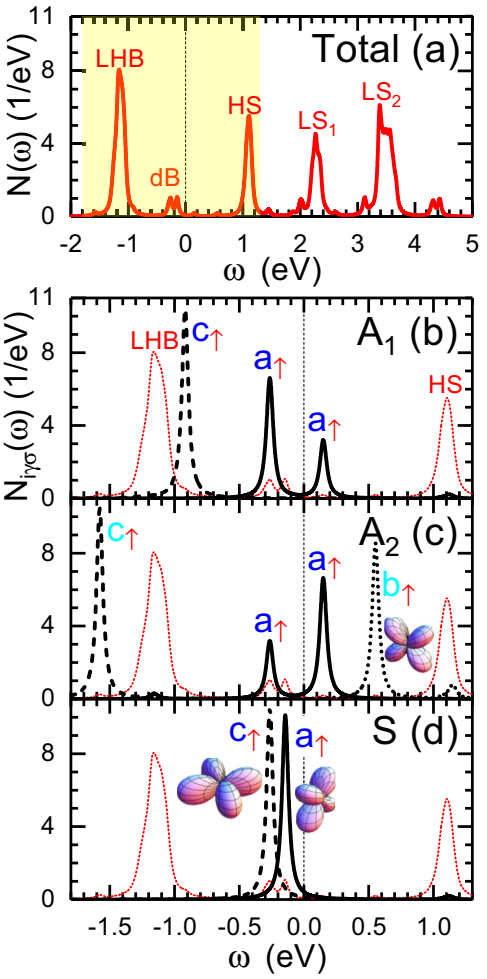

FIG. 13. Single-particle excitations: (a) Multiplet structure (total) in the presence of well annealed, or equivalently short-range-potential random, charged defects, in yellow the energy region reported in the other panels; [(b) and (c)] partial spectral weights $N_{i\gamma\sigma}(\omega)$ for vanadium ions A_1 and A_2, respectively, that belong to the active bond, and (d) for an occupied spectator site S as defined in Fig. 4. The hole is predominantly at A_2. In (b)–(d), the thin dashed red curves represent the total DOS [from (a)] and are given as reference. Parameters as in set B of Table I and $t = 0.2$ eV.

distribution of the single a electron on the active bond $\langle A_1, A_2\rangle$. In Fig. 13, the hole is mainly at site A_2 and, therefore, the c electron there is at a lower energy as it does not acquire the Hubbard interaction $(U - 3J_H)$ due to the smaller density of a electrons at site A_2. The position of the satellite c^* coincides with the occupied c level at site A_2 and therefore monitors the polarity of the active bond and, in the disordered case, the random fields of the further distant defects.

Hole delocalization on the active bond with increasing t reduces the energetic distance between the LHB and the satellite state c^*, see Fig. 12. As we have explained above, see Eq. (4.6), this δ-dependent energy shift by $[V_{\rm D} - (U - 3J_H)(1-\delta)]$ is a fraction of the Coulomb energy $(U - 3J_H)$ and is therefore much higher than t itself. In the considered example in Fig. 12, one finds the value $E_m^{(1)} \simeq -1.6$ eV for $t = 0.2$ eV which implies a hole delocalization on the active bond corresponding to $\delta \approx 0.3$. Thus

the distance of the c^* excitation can be used to probe the delocalization of the doped hole on the active bond. As the delocalization is controlled by the interplay of the kinetic matrix element t and the random defect fields, the $d^1 \rightarrow d^0$ excitation energies provide a direct measure of the strength and the fluctuations of the random fields.

So far, we have focused on the multiplet structure and on the d^1 defect state that gives rise to a satellite on the low energy side of the LHB, and should appear as $d^1 \rightarrow d^0$ transition in PES. The observation of the satellite would yield valuable information about the defect structure and the disorder strength. In the next section, we turn to further defect related transitions, namely the $d^2 \rightarrow d^1$ transitions in PES and $d^1 \rightarrow d^2$ transitions in IPES. The corresponding electron removal and addition energies fall inside the fundamental MH gap and lie below and above the chemical potential, respectively.

V. MECHANISMS FOR DEFECT STATES GAP

The most important features triggered by the presence of charged defects in the system are the (defect) states that appear within the MH gap as they determine the position of the chemical potential and the transport properties of the material. Such states originate from the LHB and, being repelled by effectively negative defects (for instance, Ca^{2+} ions substituting La^{3+} ones), are pushed upwards in energy into the MH gap. The distribution $N_0(\omega)$ of the bare electron energies h_i, as defined in Eq. (2.2), is determined by the Coulomb potentials of the random Ca^{2+} impurities. An example is shown for doping $x = 10\%$ in Fig. 14(a). The total distribution of electron energies $N_0(\omega)$ [see Fig. 14(a)] can be decomposed into the distribution $N_d(\omega)$ of energies of the V sites that are direct neighbors of at least one defect, i.e., within distance d, while the remaining V sites contribute to the second distribution $N_{nd}(\omega)$ that lies at lower energy, as shown in Figs. 14(c) and 14(d), respectively.

Figure 14 highlights three important points: (i) as there are eight vanadium sites close to each defect, but only a single hole per defect, the number of defect states is much larger than the number of doped holes; (ii) hence, the chemical potential μ lies in the high energy tail of the defect state distribution $N_d(\omega)$ [see Fig. 14(d)]; (iii) the defect states distribution below μ is not well separated from the states of the original LHB. The latter point, namely that the defect states in the Hubbard gap below μ and the LHB states cannot be easily distinguished, is a common feature of $N_0(\omega)$ and of the total DOS $N(\omega)$ of the system studied in the previous section (see Fig. 6). On the contrary, above μ, that is in the IPES regime, the defect states and the HS Hubbard band states appear well separated in energy.

The opening of a soft DS gap at the chemical potential μ in $N(\omega)$ is the most striking difference with respect to the bare DOS $N_0(\omega)$. Figure 6 displays the pronounced depletion of the DOS $N(\omega)$ right at the chemical potential (i.e., within the defect states band) for a system with long-range e-e interactions ($\eta = 1$) and several doping concentrations. One well-known mechanism for the opening of a soft gap is the combined action of long range e-e interactions and disorder as pioneered by Pollak [77] and by Efros and Shklovskii [78,79] and denoted

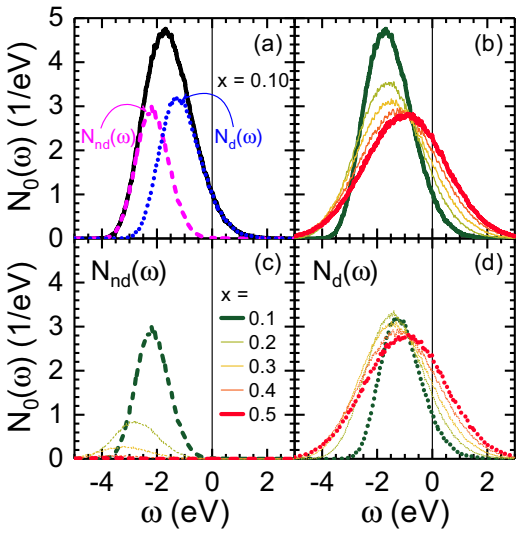

FIG. 14. Distribution of the local energies h_i due to the random defect potentials. (a) The total distribution of levels $N_0(\omega)$ (solid black line) for a doping concentration $x = 10\%$ is subdivided in a distribution $N_d(\omega)$ of energy levels of V sites that are direct neighbors of at least one defect (dotted blue line) and a remaining distribution $N_{nd}(\omega)$ of levels related to V sites that are not nearest neighbor of a defect (dashed magenta line). (b) $N_0(\omega)$, (c) $N_{nd}(\omega)$, and (d) $N_d(\omega)$ for doping concentrations x from 10% to 50% (green to red lines). The chemical potential μ (corresponding to $\omega = 0$) lies in the high energy tail of the level distribution $N_d(\omega)$ related to V sites that are nearest neighbor of a defect.

as the Coulomb gap [78]. The Coulomb gap arises from a subtle optimization of the occupation of randomly distributed localized electron states, viz. the CG model, where the total energy is minimized by the formation of a soft gap around the chemical potential.

An alternative mechanism for the formation of a gap in cubic oxides in the presence of charged defects was reported in a recent study [63,91]. In these systems, the gap arises because the doped holes: (i) are bound to the defects by the defect potential whereas the spin-orbital order greatly reduces the already constrained (2D) mobility; (ii) are confined to one of the vertical bonds of the defect cube hosting them by the in-plane AF spin order; (iii) can gain kinetic energy, leading to a splitting of the topmost occupied states, *delocalizing* over that vertical bond. That is, the system gains energy by opening a gap at the chemical potential as in the Peierls effect. However, here the splitting does not arise from an induced lattice distortion, but from the formation of bonding and anti-bonding states on the FM active bond $\langle A_1, A_2 \rangle$ close to a defect in the presence of a doped hole, as it is depicted in Fig. 13. The formation of a *kinetic* gap between the $|a\uparrow\rangle$ states in Fig. 13 is controlled by an interplay of doped holes with spin and orbital degrees of freedom, and most importantly it is controlled by the random potentials of the defects and the e-e interaction. Furthermore, it was found that the kinetic gap is not destroyed by disorder if t is large enough [63].

For a general case, it was pointed out that the kinetic and the Coulomb gap mechanisms, the latter emerging from e-e interactions, enhance jointly the DS gap in the vanadates [91].

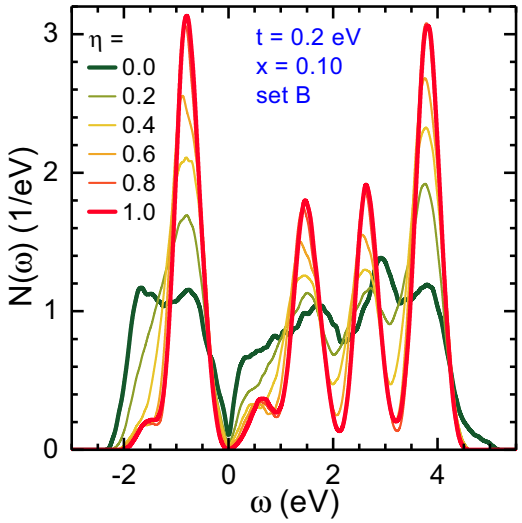

FIG. 15. Variation of the density of states and of the defect states gap for parameter set B of Table I as a function of the strength of e-e interactions $\eta = 0$, 0.2, 0.4, 0.6, 0.8, 1.0, $t = 0.2$ eV, and $x = 0.10$.

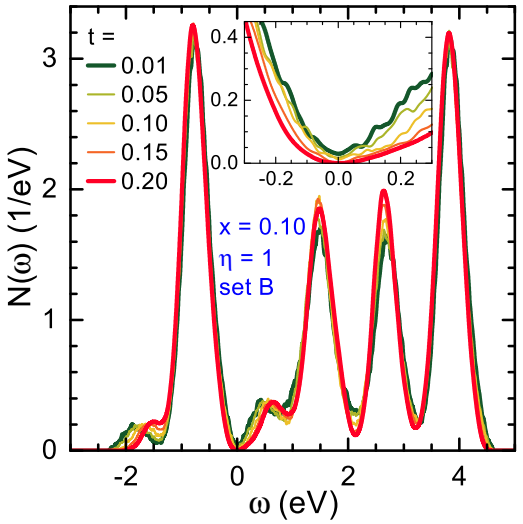

FIG. 16. Variation of the density of states and of the defect states gap for parameter set B of Table I for $t = 0.01$, 0.05, 0.10, 0.15, and 0.20 eV, $\eta = 1$, and $x = 0.10$. Inset shows the zoom of the DOS near the Fermi energy at $\omega = 0$.

We note that this is in contrast to the Anderson-Hubbard model with long-range e-e interactions where the kinetic energy suppresses the DS gap [83].

Here, we present a systematic analysis of how the e-e interactions and the kinetic-gap mechanism jointly contribute to the formation of the DS gap. In Fig. 15, for a system with doping $x = 10\%$, we investigate how the DOS $N(\omega)$ varies when the e-e interaction is switched on while keeping the value of the hopping integral $t = 0.2$ eV fixed. This is done by changing the η parameter from zero to one; notice that this corresponds to the line BC in Fig. 1. At $\eta = 0$, the quite large width of the Hubbard bands is due to the effective distribution of the levels generated by the Coulomb potentials of the random defects (see Fig. 14). With increasing η, such monopolar potentials ($\propto 1/r$) are more and more compensated by the e-e interaction. In the case $\eta = 1$, i.e., in the physical case, each single defect and the related bound hole act overall as a dipole ($\propto 1/r^2$) and, as a consequence, the effective distribution of the random energy levels gets narrower while keeping the defect positions unchanged. In Fig. 15, there is already a kinetic gap even in the complete absence of e-e interactions ($\eta = 0$). This gap is approximately linear in ω as we shall see in the statistical analysis below. With increasing η, a pronounced soft gap evolves, that can be attributed to the Coulomb gap mechanism.

In Fig. 16, we study the t dependence at $\eta = 1$, i.e., in presence of e-e interactions, for doping $x = 10\%$. This corresponds to the line DC in Fig. 1. The DOS changes only slightly as a function of t as the width of the Hubbard bands is essentially determined by the disorder. The evolution of the DS gap is amplified in the inset of Fig. 16. Surprisingly, we see here that, at small values of t, the Coulomb gap mechanism in these systems is not strong enough to create a soft gap. In a certain range $t \leqslant t^*$, the data in the inset suggest that the DOS at μ is finite. As there is nevertheless a strong suppression of the DOS we call this a pseudogap. With increasing t, the pseudogap changes into a soft gap with $N(\mu) = 0$. We shall see below by a rigorous statistical analysis that for small t values there is in fact a weak singularity with $N(0) = 0$ hidden in these data. As a side remark, we note that, with increasing t, the satellite c^* gradually moves upward. The upward shift is connected with the increasing delocalization of the hole on the active bond, as discussed above.

To analyze the behavior of the soft gap in $N(\omega)$ without suffering from the unavoidable broadening of delta functions, we consider the averaged integrated DOS $n(\omega)$, Eq. (4.4), that can be studied without artificial broadening. It is worth noting the following key features of $n(\omega)$ in the vicinity of the Fermi energy: (i) at the chemical potential there is an evident gap/plateau for $t = 0.2$ eV and $\eta = 1$ (see Fig. 7), but not for $t = 0.01$ eV, and (ii) on decreasing the screening $\eta \to 0$, the gap/plateau disappears even for $t = 0.2$ eV.

In order to establish the statistical behavior of $N(\omega)$ at low energy in the limit of an infinite number of defect realizations $M \to \infty$, we use that $N(\omega)$ is proportional to the probability distribution function $P^*(\omega)$ that the topmost occupied state (the lowest unoccupied state) in a generic defect realization s has energy $\omega = \Delta_s(-\Delta_s)$ relative to its Fermi energy μ_s. This is equivalent to the distribution of the nearest neighbor level spacings $2\Delta_s$ across the chemical potential. In Ref. [63], it has been shown that a generic defect realization features a gap of size E with a probability governed by a Weibull probability distribution function,

$$P_W(E) = \theta(E-\zeta)\,\frac{k}{\lambda}\left(\frac{E-\zeta}{\lambda}\right)^{k-1} \mathrm{e}^{-(\frac{E-\zeta}{\lambda})^k}, \qquad (5.1)$$

with shape parameter k, scale parameter λ, and location parameter ζ. Accordingly, if $\zeta = 0$, we have $P^*(\omega) = \frac{k}{\lambda^k}|\omega|^{k-1}$ and $N(\omega) \propto |\omega|^{k-1}$ both for $|\omega| \ll \lambda$. The exponent k allows to distinguish the following cases: a soft gap for $k > 2$, a linear gap for $k = 2$, a pseudogap (or singular gap) regime for $1 < k < 2$, and no gap for $k = 1$.

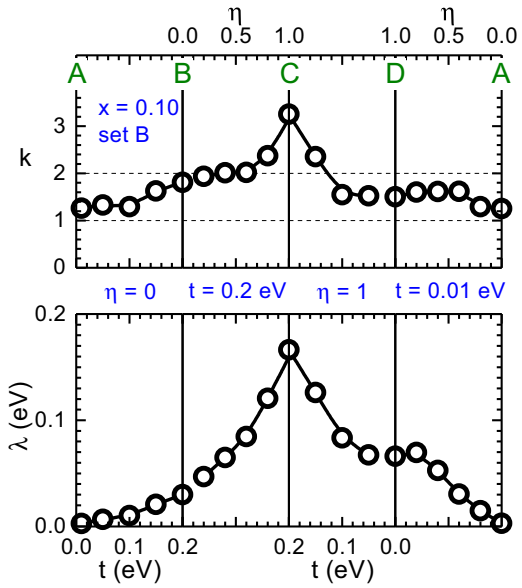

FIG. 17. Shape k (top) and scale λ (bottom) parameters of the Weibull distribution (5.1) that characterizes the soft gap at μ as a function of e-e-interaction strength η for $t = 0.2$ eV (BC) and $t = 0.01$ eV (DA), and as a function of t for $\eta = 0$ (AB) and $\eta = 1$ (CD), respectively, at $x = 0.10$. For labels A–D see Fig. 1.

Moreover, if $\zeta > 0$, the Weibull probability distribution describes a real gap, that is, in this case we have $N(\omega) = 0$ for $|\omega| \leqslant \zeta$ and $N(\omega) \propto (|\omega| - \zeta)^{k-1}$ for $\zeta < |\omega| \ll \lambda$. Thus $P_W(E)$ results in a robust scheme to determine the behavior of $N(\omega)$ close to the Fermi energy, that is, the presence and type of the overall gap in the system (through k and ζ) as well as the typical scale of the microscopic gap developing locally in the system because of all microscopic mechanisms at work (through λ).

The numerical data for the exponent k and the scale parameter λ obtained from the statistical analysis of $M = 100$ defect realizations are summarized in Fig. 17, top and bottom, respectively. The odd panels show the t dependence for $\eta = 0$ (panel AB) and 1 (panel CD), respectively, and the even panels show the η dependence for $t = 0.2$ eV (panel BC) and $t = 0.01$ eV (panel DA), respectively. The parameters k and λ are determined by a statistical least-squares fit to $P_W(E)$ of the actual distribution of gaps ($2\Delta_s$) among 100 defect realizations and yield for all cases a vanishing real gap, i.e., $\zeta = 0$. In the top panel of Fig. 17, we recognize a strong variation of the exponent $\nu = k - 1$, which determines the low frequency ($\omega \ll \lambda$) behavior of the DOS: $N(\omega) \propto \omega^{\nu}$, with the increasing/decreasing hopping or e-e interactions, t and η. This is in striking contrast to the CG model studied by Efros and Shklovskii [78,79], where $\nu = d - 1$ is determined by the spatial dimension d alone.

The size of the pseudogap is controlled by the scale parameter λ in Fig. 17 (bottom panel). In the absence of e-e interactions $\eta = 0$ (interval AB), the disorder is very strong indeed leading to a complete suppression of the soft gap in the entire range of t and to the vanishing of λ scale in the limit $t \to 0$. In panel BC, that is on increasing e-e interactions, we see an increase of k from 2 at B, which corresponds to a gap linear in $|\omega|$, as seen in the DOS in Fig. 15, to a soft gap with $k \approx 3$ at C. The increase of λ from D to C, that is on increasing t, displays the kinetic gap mechanism. Panel DA ($t = 0.01$ eV) shows that e-e interactions (in the realistic range) are not strong enough to open a soft gap when approaching the atomic limit. When approaching the point A (at $\eta = 0$) ν tends to zero, although our result for $t = 0.01$ eV is not exactly zero.

Yet as the scale parameter $\lambda \to 0$, we conclude that in the absence of e-e interactions there is a constant DOS at μ in the atomic limit. It is worth noting that, for a range of η values and t values at $\eta = 1$ around the D point (panels CD and DA), we find a pseudogap with an exponent $\nu \simeq 0.5$–0.6. This Coulomb anomaly for a 3D system is a feature distinct from the soft gap in the Efros-Shklovskii theory for the Coulomb glass and reminiscent of the Coulomb anomalies discussed for the electron gas by Altshuler and Aronov [76].

In this section, we have seen that even in the absence of e-e interactions a sufficiently large hopping t can open a gap in the defect states that survives the disorder fluctuations. However, we also found that e-e interaction alone may not be strong enough in the vanadium perovskites for the emergence of a soft DS gap with a vanishing DOS at μ. The Weibull exponent k is the largest when both mechanisms, i.e., kinetic gap formation and e-e interactions, act together. In contrast to the Efros and Sklovskii theory, we found here that the soft gap exponent $\nu = k - 1$ of the DOS at the chemical potential is nonuniversal but depends both on t and η. Next, we shall explore in detail the localization of electron states in the presence of charged defects and, in particular, the role of e-e interactions.

VI. INVERSE PARTICIPATION NUMBER AND LOCALIZATION

In this section, we determine the degree of localization of the electronic wave functions quantitatively. As useful measure of the localization of a single-particle wave function $\psi(\mathbf{r})$, the inverse participation number (IPN), $P^{-1} = \sum_i |\langle\psi|i\rangle|^4$, has been introduced for models with one orbital and one spin per site i, where the wave function $\psi(\mathbf{r})$ is assumed to be normalized. The participation number P provides a measure of the number of sites over which the single particle wave function $\psi(\mathbf{r})$ roughly extends [127]. The IPN was first considered by Bell and Dean [100] in the context of the localization of lattice vibrations and subsequently explored by Thouless [101], Wegner [102] and others [83,128,129] in the context of the Anderson localization of electronic states. The IPN has also been employed in studies related to quantum spin chains [130] and many-body localization [131].

For systems with spin and orbital degeneracy, which are of interest here, we shall define the IPN as

$$P^{-1} = \sum_i \left(\sum_{\alpha,\sigma} |\langle\psi|i,\alpha,\sigma\rangle|^2 \right)^2, \tag{6.1}$$

where the internal sums in α and σ are over local orbital and spin degrees of freedom, respectively, while the remaining sum in i is over all N sites in the system. The wave function is assumed to be normalized, i.e., $\sum_{i,\alpha,\sigma} |\langle\psi|i,\alpha,\sigma\rangle|^2 = 1$. For a localized state $\psi(\mathbf{r})$ that extends over few sites, the participation number P is a small number slightly larger than

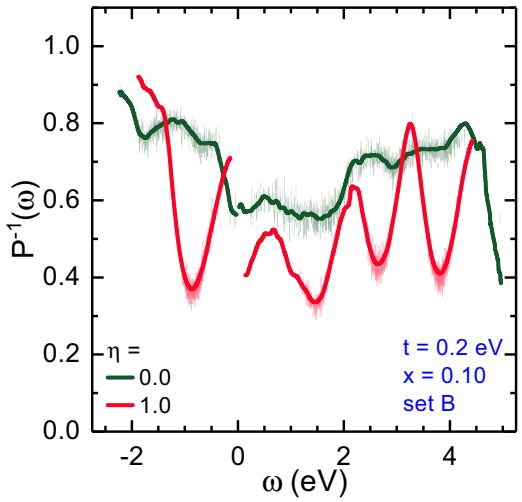

FIG. 18. Spectral function of the inverse participation number $P^{-1}(\omega)$ (6.2) for parameter set B of Table I and $t = 0.2$ eV at $x = 10\%$. The thick red curve stands for the fully screened case $\eta = 1$ and reveals a discontinuity at μ, whereas, in the absence of e-e interactions ($\eta = 0$, thick green curve), the states directly below and above μ have the same spatial extension. Thin lines stand for the average $P_n^{-1}(\omega)$ vs $\omega = \langle\omega_n\rangle$.

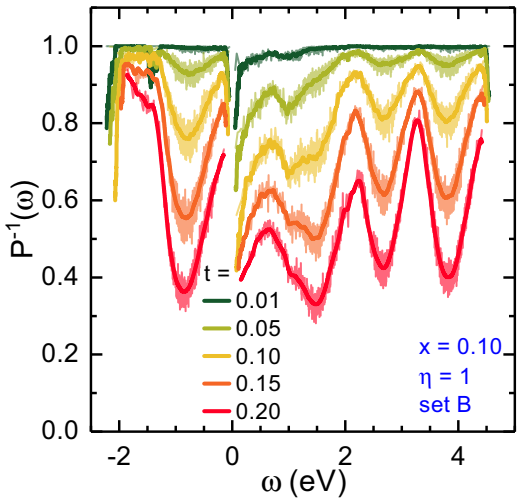

FIG. 19. Spectral function of the inverse participation number $P^{-1}(\omega)$ (6.2) for parameter set B of Table I, $t = 0.01$, 0.05, 0.10, 0.15, and 0.20 eV (green to red) and $\eta = 1$ at $x = 10\%$ (thick lines). Thin lines stand for the average $P_n^{-1}(\omega)$ vs $\omega = \langle\omega_n\rangle$.

1, whereas for an (almost) completely delocalized state (e.g., a Bloch state), it is of order N, the number of sites in the system.

Here, we are interested in the localization of the n-th HF eigenstate $\psi_{n,s}(\mathbf{r})$ corresponding to the nth HF eigenenergy $\omega_{n,s}$ both computed for the defect realization s. Therefore we shall explore the spectral function representing the statistically averaged IPN,

$$P^{-1}(\omega) = \frac{1}{M}\sum_{s=1}^{M}\left[\frac{1}{N_s(\omega)}\sum_n P_{n,s}^{-1}\delta(\omega-\omega_{n,s})\right], \qquad (6.2)$$

where $P_{n,s}^{-1}$ is the IPN computed for $\psi_{n,s}(\mathbf{r})$ and $N_s(\omega)$ is the DOS of the s defect realization. It is worth noting that the division by $N_s(\omega)$ is problematic in regions with small DOS, which are of particular interest to us. Therefore we analyze the essentially equivalent quantity,

$$P_n^{-1}(\omega = \langle\omega_n\rangle) = \frac{1}{M}\sum_{s=1}^{M} P_{n,s}^{-1}, \qquad (6.3)$$

where $\langle\omega_n\rangle = \frac{1}{M}\sum_{s=1}^{M}\omega_{n,s}$. This quantity has the great advantage to avoid the pathological division by the DOS $N_s(\omega)$ and displays in addition the fluctuations due to the many defect realizations in $\{P_{n,s}^{-1}\}$ and in $\{\omega_{n,s}\}$.

The fluctuations of the inverse participation number P_n^{-1} turn out surprisingly small as can be seen in Fig. 18, which displays two data sets, one without ($\eta = 0$) and another with ($\eta = 1$) e-e-interactions. At first glance, it is clear that both sets represent well localized wave functions over the whole spectrum. Note that a value $P^{-1} \approx 0.5$ corresponds to a wave function delocalized over two sites. It is important to note here that the localization is entirely due to the disorder, as a calculation without any defects yields $P^{-1} \approx 1/L^2$ (not shown), where L is the linear dimension of our cluster. The $1/L^2$ dependence is consistent with the 2D nature of Bloch states of the t_{2g} electrons in our system.

The striking difference of the two data sets in Fig. 18 reflects the absence or presence of the screening by t_{2g} electrons. Without e-e interactions, the monopolar defect potentials are not screened and hence the disorder effect is stronger; this is already manifest in the larger width of the LHB in the DOS. In the screened case instead, the Hubbard bands are much narrower in the DOS, but also in the IPN distribution. The smaller values of IPN in the center of the Hubbard bands for $\eta = 1$ indicate that these states are definitely more delocalized when the defect potentials are screened. In the $\eta = 1$ case, it is worth noting that the defect states are much more localized, for instance in the energy region of the c^* satellite, in comparison to the states in the center of the Hubbard bands, which are less affected by the random defect potentials and therefore show a smaller IPN.

The IPN of defect states inside the MH gap shows several interesting features. In the unscreened case $\eta = 0$, the inverse participation number is approximately constant ($P^{-1} \approx 0.6$) for the states close to the chemical potential. This case corresponds to the DOS linear in ω in Fig. 15. For the screened case $\eta = 1$, however, we observe a pronounced discontinuity in the degree of localization of defect states right below and above μ, as seen in Fig. 18. The discontinuity in the degree of localization of the defect states at the chemical potential reflects the different nature of the electron removal and addition states in presence of e-e interactions. It is evident from Fig. 18 that the removal states are more localized than the addition states.

In Fig. 19, we explore the t dependence of the IPN for the case with e-e interactions ($\eta = 1$). We recognize that in the regime of small t (close to the atomic limit) $P^{-1} \approx 1$. That is the electron states are perfectly localized at a single site, as one expects for the classical case $t = 0$. The upper limit $P^{-1} = 1$ shows that our definition of the IPN in the spin and orbital degenerate case is correct. The choice of a small finite hopping $t = 0.01$ eV in Fig. 19 is dictated by the dependence on t of

the computation time: the smaller t is the longer it takes to reach convergence. We see that the defect states close to μ and those at the bottom of the LHB are slightly more delocalized. For these defect states, IPN is in the range $P^{-1} \in (0.8, 1.0)$. This weak delocalization at small t is a consequence of the motion of the holes on the active bonds and increases with increasing t. We also see that the states in the center of the various Hubbard subbands delocalize faster with increasing t than the defect states in between the Hubbard multiplets. Thus we can conclude that all states remain well localized even at the moderate doping concentration of $x = 10\%$ and for the typical value $t = 0.2$ eV of the hopping integral in these materials.

VII. SPIN-ORBITAL POLARONS AND REDUCTION OF MAGNETIC AND ORBITAL ORDER

From the study of the IPN in the previous section, it naturally follows that (i) the defect states must be visualized as localized small polaron states that are tightly bound to defects and (ii) the symmetry of each polaron state relative to the closest defect must be strongly broken. It is important to contrast here two distinct physical sources of *localization* in condensed matter physics.

(1) Wave functions *localize* (i.e., their spatial extension undergoes an extreme reduction) due to the presence of defects or of any kind of disorder, as it happens, for instance, to the single particle states in the Anderson localization scenario [74,75].

(2) On the other hand, electrons *localize* also due to strong (local) e-e interactions as in the half-filled Hubbard model, that is in the absence of disorder [132].

In general, the Anderson and the Mott routes to localization, as listed above, are expected to combine in very nontrivial ways [133]. In the regime of strong correlations, $t \ll U$, the ground state of the Hubbard model at half-filling is a Mott insulator with AF spin correlations. Added holes create spin defects while moving in the AF spin background, and form spin polarons [134,135]. The motion of the hole inside the polaron cloud represents the main kinetic energy. Yet, as found for instance in the high-T_c materials, the entire polaron may in addition perform a coherent motion on the magnetic energy scale $J \propto t^2/U$ [134].

In the case of orbital polarons in a state with AO order, the holes have an even stronger tendency towards localization, for instance in systems with t_{2g} orbital degrees of freedom [109,136,137]. A similar analysis of individual hopping processes as for spin polarons [135,138] is possible and provides a good insight both into the optical excitations [139] and the spectral properties [23,140–142] of orbital systems. More demanding is the theoretical description of a charge added to a system where both spin and orbital order alternates and excitations of both types of degrees of freedom may contribute to the polaron cloud [62,143]. Results depend on the actual symmetry of the spin and orbital order realized in the ground state. Theoretical studies have shown that single SO polarons in systems where both spins and t_{2g} orbitals alternate, as in the (a,b) planes of the vanadium perovskites, tend to localize [60,61].

Experimentally, such polarons were first identified in half-doped manganites for e_g orbital degrees of freedom [144,145], but exist also in doped cobaltates [59] and in the cubic vanadates [58]. In the latter case, being of interest here, the doped holes move in the spin-orbital ordered C-AF/G-AO state and the emerging SO polarons perturb both spin and orbital order. These polarons are bound to the charged defects: this eliminates any coherent motion and the perturbation of the spin-orbital order in the system can be described by means of a detailed analysis of the nature and of the structure of the polaron cloud, see below. Thus the polaron cloud provides a many-body measure of the reduction of the spin- and orbital-order parameter as a function of doping. In this section, our aim is to define the SO polaron wave function and to explore the spatial extension, or the IPN of the SO polaron.

In the spin- and orbital-ordered state, it is convenient to expand the polaron wave function $|\psi_n(i)\rangle$ in a *string* basis,

$$|\psi_n(i)\rangle = \sum_{\delta,\alpha} a_{n,\alpha}(\delta)|i+\delta; S_\alpha(\delta)\rangle, \tag{7.1}$$

where the label n distinguishes polaron states that may differ by their spatial symmetry and their spin. However, in the following, we shall consider only the polaron state with the minimal energy. The wave function of the polaron $|\psi_n(i)\rangle$ is centered or has its largest amplitude at the vanadium site i. Its kinetic energy involves the neighboring sites $\{i+\delta\}$, on varying $\delta = \sum_{m=1}^{n(\alpha)} \delta_m$, as the hole propagates along different paths, $S_\alpha(\delta) = \{\delta_1, \delta_2, \ldots, \delta_{n(\alpha)}\}$, where $\delta_m = \pm e_\nu$ and $\nu = x, y, z$ are the unit vectors of the cubic lattice. A string state, $|i+\delta; S_\alpha(\delta)\rangle$ in Eq. (7.1), corresponds to the state of a hole after it has moved along a particular path $S_\alpha(\delta)$ from site i to site $i+\delta$ and, therefore, it automatically contains information about the spin and orbital defects created along that particular path. Next, we proceed as in the case of the localization of single particle wave functions and define the IPN for the many-body wave functions of SO polarons as

$$P_n^{-1} = \sum_{\delta} \left(\sum_{\alpha} |a_{n,\alpha}(\delta)|^2 \right)^2. \tag{7.2}$$

As each path $S_\alpha(\delta)$ corresponds to a sequence of spin-flips and/or orbital changes relatively to the underlying spin-orbital ordered background, the energy of a string state increases with the length of the related path and only short paths and related string states contribute effectively as long as the system is not close to a phase transition.

In the dilute case (i.e., small density x of doped holes), the overall reduction of the local magnetic order parameter m^s can be calculated from the spin deviation m^{sP}, with respect to the underlying spin-orbital ordered background associated with a single polaron,

$$m^s \simeq m_0^s - x m^{sP}, \tag{7.3}$$

where m_0^s is the local magnetization in the undoped ground state, as we can imagine that the interactions between polarons are negligible. Then, m^{sP} can be computed by means of the many-body wave function of the SO polaron,

$$m^{sP} = \langle\psi_0|\hat{m}^s(Q)|\psi_0\rangle - \langle\psi(i)|\hat{m}^s(Q)|\psi(i)\rangle. \tag{7.4}$$

Here, $|\psi_0\rangle$ is the N-particle ground state of the underlying spin-orbital ordered background and $|\psi(i)\rangle$ is a single-polaron wave function in the space of $(N-1)$ particles.

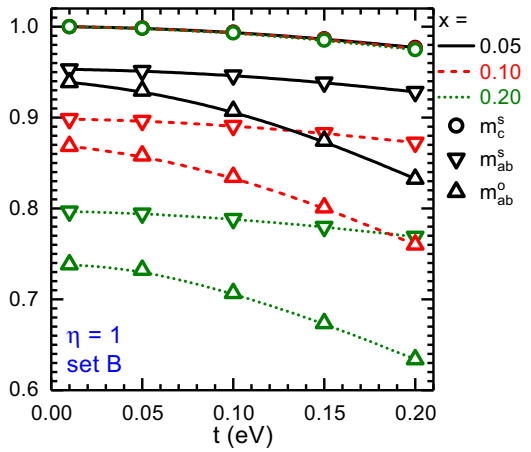

FIG. 20. Self-consistent uHF results for the spin-order parameters m_c^s and m_{ab}^s and the orbital-order parameter m_{ab}^o for the C-AF/G-AO ordered phase resulting from electrons in a/b and c orbitals, respectively, as functions of the hopping parameter t and for different doping concentrations $x = 0.05, 0.10, 0.15$.

In this section, we analyze the localization from the strong correlation perspective. It is evident from the uHF results for the IPN in Fig. 19 that all states of the system are perfectly localized in the limit $t \to 0$. With increasing t the states become gradually more extended. Accordingly, an important probe for the delocalization is the decrease of spin and orbital order parameters m^s and m^o, respectively. The staggered spin order of the C-AF structure, for example, is measured by

$$\hat{m}_\nu^s(\boldsymbol{Q}) \equiv \sum_j \hat{m}_{j,\nu}^z e^{i\,\boldsymbol{Q}\cdot\boldsymbol{j}}, \tag{7.5}$$

where $\boldsymbol{j}$ and $\nu = a, b, c$ are site and orbital flavor indices, respectively. In the following, we use the convention $\hat{m}^z = 2\hat{S}^z$, where $\hat{S}^z$ is the z component of a spin-1/2 operator. The staggered orders of C and G states are measured by modulation vectors $\boldsymbol{Q}_C = (\pi,\pi,0)$ and $\boldsymbol{Q}_G = (\pi,\pi,\pi)$, respectively. Furthermore, within the uHF approach, it is straightforward to distinguish the contributions from ab and c electrons to the order parameters, respectively. Thus

$$m^s = m_{ab}^s + m_c^s, \tag{7.6}$$

where $m_\nu^s = \langle \hat{m}_\nu^s(\boldsymbol{Q}_C)\rangle$ for C-type spin order. Similar construction applies for the G-type orbital order parameter, $m_\nu^o = \langle \hat{m}_\nu^o(Q_G)\rangle$.

In Fig. 20, the t dependence of the spin-order parameters m_{ab}^s and m_c^s and of the orbital-order parameter m_{ab}^o are shown. As we already explained above, hole doping concerns the $\{a,b\}$ orbital doublet and the magnetic moment component m_{ab}^s is thus reduced by x at $t = 0$, whereas $m_c^s = 1$ remains unchanged as there is no doping into c orbitals. On increasing t, holes move and the spin and orbital order are further reduced. This effect is particularly small for c orbitals, as their motion involves only doubly occupied c^2 configurations and, therefore, costs the intraorbital Hubbard repulsion U. The contribution of such processes is small in comparison to that of the virtual processes involving a and b electrons. In Fig. 20, one recognizes a strong reduction of the orbital order m_{ab}^o, both as a function of x and t. In fact, the kinetic processes have a stronger effect on the G-type orbital order parameter m_{ab}^o than on the C-type spin order m_{ab}^s. This may be seen as a precursor of the trend observed in the experiments performed on $La_{1-x}Sr_xVO_3$ [55] where the G-AO order melts at a lower doping than the C-AF spin order.

Next, we shall use the order parameter expressions, derived in Appendix B by assuming noninteracting small SO polarons, for the interpretation of the uHF results. The central assumption is the linearity in x of the order parameter corrections, which is confirmed by the present uHF results in a wide doping range, see Appendix B. It is important to recognize that in the insulating regime that we are considering, each small polaron is bound to and strongly deformed by the central charged defect. Thus the number of relevant paths for the doped holes are significatively reduced in comparison to those available for a polaron not attached to a defect. Furthermore, the polaron state is strongly influenced by the random fields resulting from the other more-distant defects.

The expressions for the spin and orbital deviations associated with a single polaron are derived by considering the polaron cloud of a hole located on an active bond close to a defect. It is the FM correlations along the c direction in C-AF structure in combination with the defect potential, which defines the direction of the active bond, that yield the dominant gain of kinetic energy for the hole. The virtual motion of holes in a or b direction is instead quenched by AF correlations. Thus the polaron wave function is characterized by two physical parameters, namely: (i) the polarity parameter of the active bond δ_c, where $\delta_c = 0$ describes a hole localized on a single site, as for $t = 0$, and $\delta_c = 1/2$ an equal partition between the two sites of the active bond, as in the case of large t and screened far-defect potentials ($\eta = 1$); (ii) the activation energy e_0 of the virtual string excitations. We focus here on the spin- and orbital-order parameter due to a/b orbitals that show the strongest dependence on doping:

$$\begin{aligned} m_{ab}^s &\cong 1 - x\left[1 + \frac{2(t/e_0)^2}{1+(t/e_0)^2}\right], \\ m_{ab}^o &\cong 1 - x\left[1 + 2\delta_c + \frac{2(t/e_0)^2}{1+(t/e_0)^2}\right]. \end{aligned} \tag{7.7}$$

For an isolated single defect, the activation energy e_0 is given by Hund's coupling J_H, whereas δ_c is controlled primarily by t and the Jahn-Teller coupling. In the presence of disorder, the potentials due to the random far defects affect quite strongly both the activation energy e_0 and the polarity parameter δ_c. Accordingly, these parameters are taken here as natural variational parameters. When we apply these relations to the uHF results, obtained as a statistical average over many defect realizations, we obtain for δ_c and e_0 the values of a *typical* bound small polaron.

Figure 21 shows the *typical* polaron parameters obtained by fitting the uHF results shown in Fig. 20 for the spin and orbital order parameters, m_{ab}^s and m_{ab}^o, see Eqs. (7.7) (see also Appendix B). We find a significant increase of the activation energy e_0 from 0.33 eV at $x = 5\%$ to 0.82 eV at $x = 25\%$. This increase can be attributed to the increase of the overall random potential strength on the single defect cube when the concentration of defects becomes larger and larger. We note that Hund's exchange, which is the energy scale e_0 for an

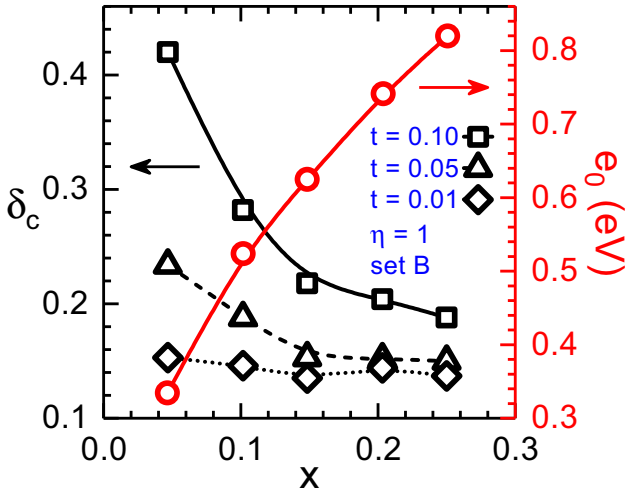

FIG. 21. Doping dependence of the polaron superexchange energy scale e_0 and of the polarity parameter δ_c of a *typical* active bond for different values of t (in eV) and parameter set B of Table I. The lines are guides to the eye.

isolated defect as already mentioned above, is $J_H = 0.6$ eV for parameter set B of Table I.

The interpretation of the data for the polarity parameter δ_c is more subtle. Here we determine δ_c directly from the data in Fig. 20 via the difference of m^o_{ab} and m^s_{ab} using Eqs. (7.7). The parameter δ_c naturally depends on x and on t; large t favors an equal distribution on the active bond, that is $\delta_c = 0.5$. At small doping, this is almost realized for $t = 0.1$ in Fig. 21 since the random polarization fields (i.e., the far-defect potentials) are quite small in this case. It is worth noting that, in the low doping regime, the small Jahn-Teller potentials, which naturally lead to an imbalance, become also relevant.

By means of the same small-polaron wave function for a hole on an active bond, we obtain for the IPN, with the help of the definition in Eq. (7.2),

$$P_a^{-1} \cong \left(1 - 2\delta_c + 2\delta_c^2\right)\left[1 - \frac{2(t/e_0)^2}{1 + (t/e_0)^2}\right]. \qquad (7.8)$$

The finite polarity parameter δ_c explains the deviation of the IPN from 1 in the small t case for the states in the soft gap close to the chemical potential (see Fig. 19). The overall t dependence of the IPN close to μ is determined both by the t dependence of the polarity parameter $\delta_c(x,t)$ and by the virtual-string contributions in the polaron wave function. Interestingly, the nonlinear corrections driven by the random polarization fields via the x dependence of e_0 and δ_c are particularly pronounced at small x values (see also Appendix B).

In this section, we have focused on the microscopic character of the defect states that are responsible for the formation of the soft gap and the reduction of spin and orbital order. We have shown that the SO polaron states inside the MH gap have a reduced spatial symmetry and are more strongly localized than the states in the center of the Hubbard bands. The polaron states in the soft gap are controlled by the randomness of the defect locations and by the interplay of kinetic energy and *e-e* interactions.

VIII. RELATION TO THE PES OF $La_{1-x}Ca_xVO_3$

Now, we turn to the questions how the structure of the DS gap is affected by the strength of the defect potential V_D and whether we can identify characteristic defect-related features in the doping dependence of existing PES data. We shall explore here the PES spectra of $La_{1-x}Ca_xVO_3$ since for this system Maiti and Sarma [69] have measured the doping dependence up to $x = 0.5$, and moreover both PES and IPES spectra exist for the parent compound $LaVO_3$ [70]. The latter yields clear evidence of the multiplet structure and provides an estimate for Hund's exchange J_H (see Fig. 2). Moreover, these spectra give us a measure for the principal parameter for the Mott gap $U - 3J_H \approx 2.7$–3.0 eV between the centers of the LHB and the HS multiplet of the UHB. In the following study, we shall use $U - 3J_H = 3.0$ eV as determined by Maiti and Sarma [70] (set C of Table I). Another important energy scale that follows from PES experiments is the distance of the chemical potential from the center of the LHB, $\mu - E_{\rm LHB}$. Surprisingly, over the whole doping range in $La_{1-x}Ca_xVO_3$, up to $x = 0.5$, this scale is approximately constant, $\mu - E_{\rm LHB} \approx 1.5$ eV. Since it is the repulsive defect potential that pulls the d^2 defect states upward out of the LHB, we expect also an upward shift of the chemical potential. Therefore the distance of the chemical potential from the LHB center is expected to scale with the parameter V_D in the Hamiltonian Eq. (2.1).

At this point, it is interesting to note that the pioneering work of Mott [132] in the 1970s on the metallic and nonmetallic states of strongly correlated matter was to some extent stimulated by the experiments of Dougier and Hagenmuller [146], who explored the electrical conductivity of $LaVO_3$ doped with strontium. The metal-insulator transition in this compound at $x_c \approx 0.23$ was attributed to an Anderson type transition between localized and delocalized states in an impurity band. The option of a Mott gap in the defect band was ruled out [147]. The presence of a soft gap with $N(\mu) = 0$ in the insulating regime has not been considered.

So far, we have analyzed spectral functions in Secs. IV–VI using parameter set B of Table I. They have the advantage that satellite structures are well resolved, representing the atomic multiplet excitations. Interestingly, we see from spectra in Fig. 6, calculated with inclusion of *e-e* interactions, that the LHB center remains at a fixed distance relative to the chemical potential for all doping concentrations, as required by the above experiments. However, parameter set B implies $U - 3J_H = 2.2$ eV and $\mu - E_{\rm LHB} \simeq 0.8$ eV being both too small and thus not appropriate for the $La_{1-x}Ca_xVO_3$ compounds.

In Fig. 22, we display the V_D dependence of the DOS for $U - 3J_H = 3.0$ eV appropriate for $La_{1-x}Ca_xVO_3$ (set C of Table I) at $x = 10\%$ doping. The resulting $N(\omega)$ spectra depend strongly on the V_D parameter, Eq. (2.3), which determines both the strength of the Coulomb-like defect potentials and the strength of *e-e* interactions, Eq. (2.4), guaranteeing charge neutrality. On increasing V_D from 1.0 to 2.0 eV, we recognize: (i) the DS gap becomes wider and softer; (ii) the characteristic energy scale $\mu - E_{\rm LHB}$ increases; (iii) the $d^1 \rightarrow d^0$ satellite moves closer to the LHB and gets gradually absorbed. Moreover, (iv) the defect states right above the chemical potential

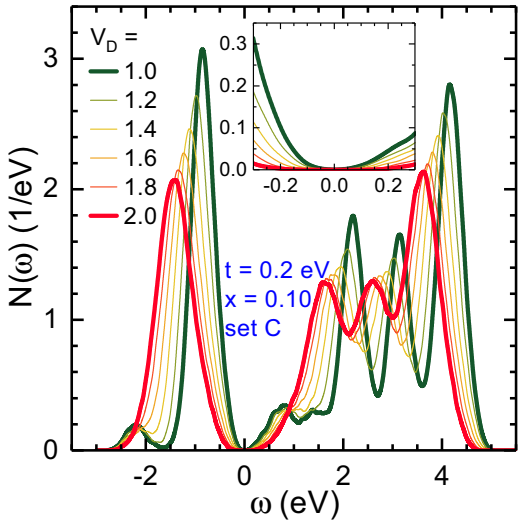

FIG. 22. Density of states for $x = 10\%$ and six different defect potentials $V_D \in [1.0, 2.0]$ eV. The data show that the distance between the LHB and the chemical potential (at $\omega = 0$) is increasing with V_D while the distance between the LHB and the HS state of the UHB stays constant. Parameters are $t = 0.2$ eV and set C of Table I. The defect potential is of Coulomb type and e-e interactions are included ($\eta = 1$).

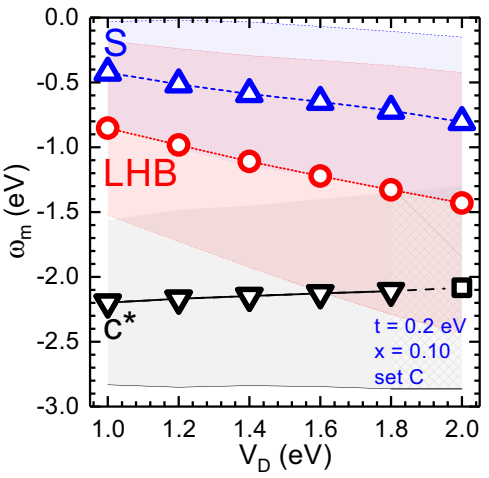

FIG. 23. Characteristic energies ω_m of the spectral features resolved below the chemical potential μ ($\omega = 0$) as functions of the defect potential $V_D \in [1.0, 2.0]$ eV: the center of gravity of the LHB (LHB, red circles), the filled defect states (S, blue up-triangles), and the satellite due to hole states (c^*, black down-triangles and square). The energies and the linewidths (indicated by the shaded areas colored according to the symbol colors) were determined by fitting the data in Fig. 22 with three Gaussians, respectively. The c^* data for $V_D = 2.0$ eV (black square) have been obtained by linear fitting the data for $V_D < 2.0$ eV as there was no possibility to resolve such peak within the overall LHB peak.

($\mu = 0$), which are well separated from the HS UHB at $V_D = 1$ eV, merge with this latter for $V_D = 2$ eV; and (v) the gaps between the multiplets of the UHB get gradually filled with defect states as V_D increases. Finally, we see that it requires a value $V_D \approx 2$ eV until one reaches the experimental value $\mu - E_{\mathrm{LHB}} \approx 1.5$ eV. One also notices in Fig. 22 that the energy between the center of LHB and the HS state of the UHB remains unchanged $U - 3J_H = 3.0$ eV for the different values of V_D, as expected from Table II. That is, the intra-atomic excitations and multiplet splittings are not affected by the disorder.

The V_D dependence of several characteristic single particle excitations ω_m relative to the chemical potential ($\mu = 0$) are plotted in Fig. 23. The characteristic energies $\omega_{\mathrm{LHB}} = E_{\mathrm{LHB}} - \mu$ as well as the satellite energies, ω_{c^*} and ω_S have been determined by a fit with three Gaussians to the spectra in Fig. 22 at negative energy. The linewidths are indicated by shading. In order to understand the variation of $\omega_{\mathrm{LHB}} = E_{\mathrm{LHB}} - \mu$ we need an estimate for the dependence of E_{LHB} and μ on the defect potential V_D. The center of the LHB corresponds to a $d^2 \rightarrow d^1$ transition. In uHF, this energy is connected with the removal of the topmost occupied a (or b) electron of a d^2 configuration far away from a defect,

$$E_{\mathrm{LHB}} \simeq \epsilon_a + U - 3J_H. \tag{8.1}$$

The chemical potential can be approximated by a similar excitation in the direct neighborhood of a defect, that is at a spectator site. Hence

$$\mu \approx \epsilon_a + U - 3J_H + V_D, \tag{8.2}$$

and therefore

$$\omega_{\mathrm{LHB}} = E_{\mathrm{LHB}} - \mu \approx -V_D. \tag{8.3}$$

This simple estimate reproduces qualitatively the trend of the full self-consistent uHF result in Fig. 23 that is $\omega_{\mathrm{LHB}} \approx -0.8 V_D$. The small deviation is not unexpected since both E_{LHB} and μ will acquire upward shifts from the long-range tails of the defect potentials leading to a small positive correction proportional to V_D in $E_{\mathrm{LHB}} - \mu$.

The satellite c^* corresponds to a $d^1 \rightarrow d^0$ transition and is a fingerprint of the spin-orbital polaron state. As we discussed before the doped hole selects an *active* FM bond $\langle i, j \rangle$ parallel to c next to a defect. The random defect fields tend to localize the hole on a single site i leading to a configuration $|c_i, (c_j a_j)\rangle$ where the single a electron is on site j of the active bond. This is described by the polarization parameter $\delta_c = 0$. If the kinetic energy (i.e., t) is strong enough, the a electron delocalizes on the active bond leading to $\delta_c = 0.5$. The annihilation energies of c electrons in the two configurations relative to the chemical potential μ are

$$\omega_{c^*} \simeq \epsilon_c - \epsilon_a - (U - 3J_H)(1 - \delta_c), \tag{8.4}$$

$$\omega_S \simeq \epsilon_c - \epsilon_a - (U - 3J_H)\delta_c. \tag{8.5}$$

Most importantly, in the expression of ω_{c^*}, the dependence on the polarization parameter δ_c contributes with a large prefactor $U - 3J_H$. Therefore the delocalization of the remaining a electron in the small polaron is reflected in a large energy shift of the c^* satellite. That is, the state of the a electron can be probed by annihilation of c electrons. Comparing the expression ω_{c^*} with the data in Fig. 23 yields $\delta_c \simeq 0.3(0.33)$ at $V_D = 1(2)$ eV, respectively. There is no direct V_D dependence in these expressions. The origin of the small change of δ_c observed above is unclear.

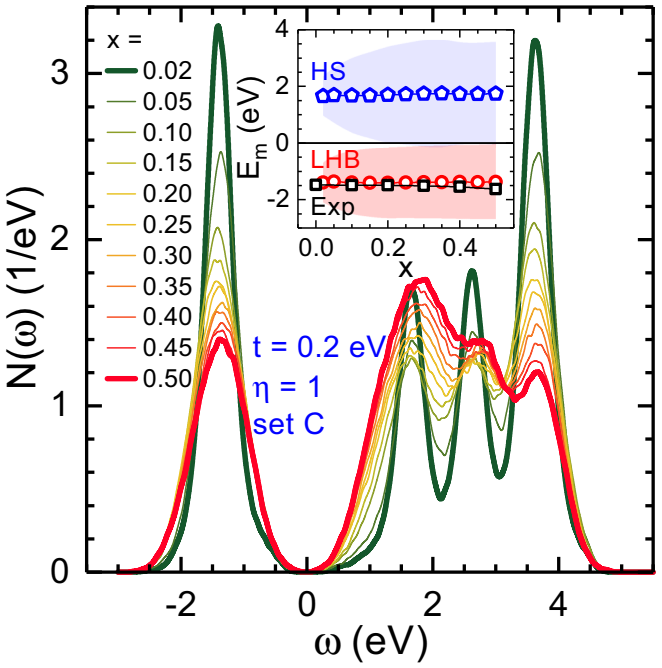

FIG. 24. Density of states $N(\omega)$ as a function of increasing doping concentration $x \in [0.02,0.50]$ for set C of Table I including e-e interactions ($\eta = 1$) and for $t = 0.2$ eV. Inset displays the small variation with x of the distance of the peak of LHB from chemical potential μ ($\omega = 0$): experimental results of Maiti, Mahadevan, and Sarma for $La_{1-x}Ca_xVO_3$ [69] (black squares); theoretical data for the LHB (red circles) and the HS state of the UHB (blue pentagons). The shaded areas colored according to the symbol colors give a measure of the linewidths of the related multiplet structures.

As one can see in Figs. 22 and 23, the widths of both the LHB and the UHB increase with increasing defect potential V_D. Since the corresponding spectra are calculated for fixed doping $x = 0.1$ and constant kinetic energy parameter t, the broadening can be directly attributed to the increasing randomness resulting from the stronger long-range disorder potentials. Moreover, we see that, at small $V_D \simeq 1.0$ eV, the $d^1 \to d^0$ satellite excitations with energy ω_{c^*} are well separated from the $d^2 \to d^1$ excitations at ω_{LHB} that define the LHB. Due to the V_D dependence of the LHB, see Eq. (8.3), the c^* satellite penetrates the LHB at $V_D \approx 1.6$ eV. In other words, the d^0 final state on the active bond becomes unstable and changes into a d^1 state by a simultaneous $d^2 \to d^1$ transition at a vanadium host site not belonging to the defect cube. With the onset of the delocalization of holes, we come to the borderline of the regime of well localized spin-orbital polarons. The delocalization of holes has severe consequences for the uHF algorithm and leads to a slowing-down of convergence of the algorithm, that is, for large V_D when the c^* satellite disappears in the LHB.

The doping dependence of the uHF DOS for $La_{1-x}Ca_xVO_3$ is displayed in Fig. 24. These calculations were performed using long-range e-e interactions ($\eta = 1$) and interaction parameters, $U - 3J_H = 3.0$ eV and $V_D = 2.0$ eV (see parameter set C in Table I). As most important features on the PES side of the spectra we note: (i) the persistence of a soft DS gap up to large doping, and (ii) the essentially doping independent distance of the chemical potential from the center of the LHB, as found in the experimental data of Maiti and Sarma [69]. Unfortunately, the existing experimental data do not allow to draw a conclusion with any certainty concerning the existence of a c^* satellite. Thus it remains as a challenge for future higher resolution experiments to see whether this feature can be resolved. The inset highlights the independence on doping of $\mu - E_{LHB} \approx 1.4$ eV and of the fundamental Hubbard gap ($U - 3J_H$). The decrease of the spectral weights with doping is consistent with the sum rules discussed in Sec. IV.

We observe a pronounced shift of spectral weight in the UHB towards lower energies as a function of doping, i.e., resulting in an increase of the spectral weight in the regime of HS excited states. At large doping, the multiplet structures of the UHB begin to merge and, as a consequence, the UHB becomes almost featureless. The multiplet excitations lose their distinct character as (for these parameters) these excitation processes are degenerate with $d^1 \to d^2$ excitations at hole sites. Moreover, we note that the $d^1 \to d^2$ transitions have a narrower width of their multiplet structure compared to that for the $d^2 \to d^3$ transitions of the host.

In Fig. 24, we recognize a moderate increase of the width of the LHB with increasing defect and doping concentration. This one may have expected since there are two prevailing mechanism that contribute to an additional broadening of the LHB when the doping concentration is increased. Namely, (i) there are the growing satellites c^* and S that contribute to increasing the overall width of the LHB, and (ii) due to the increasing doping concentration, the defects get closer and thereby the disorder fluctuations are expected to increase. There is, however, also a counteracting effect due to an increased screening resulting from the defect states and the narrowing of the soft gap. We note that this screening, which is still nonmetallic, is fully included in our calculation, due to the finite-field method we are using. We also remark that, in terms of an alternative random-phase many-body theory, our treatment of e-e interactions for the t_{2g} subsystem would correspond to the calculation of the full dielectric matrix [148] for an inhomogeneous and random system. The complex dielectric matrix would then yield a quite similar or even the same polarization charge density induced by the defect potentials as in our uHF calculations. This perspective highlights that the dielectric screening in systems with defect states and soft gaps is rather involved and, to the best of our knowledge, it has not been addressed yet by any many-body theoretical approach.

IX. DISCUSSION AND SUMMARY

This work elucidates the inherent complexity of charged defect states in orbitally-degenerate Mott insulators. We have studied a generic three-band model representing the t_{2g} electrons of the vanadium ions that guarantees a faithful description of the magnetic and orbital ordered phases of the vanadium perovskites such as $LaVO_3$ or YVO_3. The model developed here includes the local Hubbard-Hund interactions and the long-range e-e interactions. Therefore, it describes the dielectric screening of the Coulomb potentials of the random charged defects due to the t_{2g} electrons explicitly in the regime of strong electron correlations. Nevertheless, there are relevant interactions that we have omitted, such as spin-orbit and orbital polarization interactions, as discussed in Sec. II. We have

neglected such terms to achieve a closer correspondence to the generic models used in studies of disorder such as the quantum Coulomb glass or the Anderson-Hubbard model. Our model may be thus seen as multiflavor generalization of these models.

The calculation of the one-particle excitation spectra of a Mott insulator with orbital degeneracy and random defects is a complex task that was only possible to undertake within the unrestricted Hartree-Fock approximation. We stress that this is the only scheme able to (i) control simultaneously the strong correlations, the Coulomb interactions and the randomness of defects even at high doping and (ii) reproduce the essence of Mott physics, i.e., the atomic multiplet structure and the variation of the spectral weights in the Hubbard bands. A more detailed description of the algorithm used for the treatment of disorder is given in Appendix A. There, we also display a subtle convergency test for our algorithm and show that the gradual switching on and off of *e-e* interactions leads basically to the same statistical average for the density of states $N(\omega)$ as for the initial state.

An important feature of the vanadium perovskites is the robustness of the Mott-Hubbard gap and of the spin and orbital order up to high doping concentrations. Our unrestricted Hartree-Fock results for the single particle density of states $N(\omega)$ reveal the persistence of the atomic multiplet structure of V ions up to doping concentrations as large as 50% in photoemission and inverse photoemission spectra. At the same time, there is a strong spectral weight transfer from the Hubbard bands into the Mott-Hubbard gap and into satellite structures of the lower Hubbard band and the multiplets of the upper Hubbard band. We have analyzed the energetics and the doping dependence of spectral weights of the different excitations in the atomic limit that provides valuable information for the insightful interpretation of photoemission spectra.

The opening of a gap in the defect states at the chemical potential μ inside the Mott gap is a subtle feature in doped Mott insulators. We have presented a very detailed analysis how *e-e* interactions and the kinetic gap mechanism jointly contribute to the formation of the gap in defect states. As we have shown, the states in the defect states gap can be understood as small spin-orbital polaron states bound to defects. Note that, in the presence of *e-e* interactions, these objects are electric dipoles that interact effectively via dipole-dipole interactions. The kinetic energy gain of the doped hole moving within the spin-orbital polaron on a ferromagnetic active bond is the origin of a level splitting at μ and thereby of the kinetic mechanism for the defect-states gap formation. We have demonstrated that the defect-states gap survives the disorder average and typically yields a soft gap.

Central role for the quantitative description of the insulating state is played here by a statistical analysis of the gap using a Weibull distribution as introduced in Ref. [63]. Using this tool, we have shown that the exponent ν of the soft gap in $N(\omega) \propto |\omega|^{\nu}$ at the chemical potential is nonuniversal, that is, it depends sensitively on: (i) the strength of *e-e* interactions and (ii) on the hopping parameter t, which controls the kinetic energy. In particular, we note here that in the atomic limit ($t = 0$), *e-e* interactions are not strong enough to produce a Coulomb gap in the vanadium perovskites, as one might expect on the basis of Efros-Shklovskii theory. Instead, we find in this regime exponents that rather correspond to a Coulomb or zero-bias anomaly $0 < \nu < 1$.

We have investigated the degree of localization of the unrestricted Hartree-Fock wave functions quantitatively. We used here as a measure the inverse participation number, which we have generalized for systems with spin and orbital flavors. In particular, we have found that the defect states in the soft gap are typically localized on one up to two sites, and they are more strongly localized than the states inside the Hubbard bands. This feature is surprising and the inverse participation number provides an independent proof for *small* spin-orbital polarons bound to defects. Interestingly, we observed a strong discontinuity in the localization of states right below and above μ in the presence of *e-e* interactions, whereas in their absence no discontinuity could be found.

Using the unrestricted Hartree-Fock, we have calculated the doping dependence of spin- and orbital-order parameters in the C-AF/G-AO phase. Our results reveal a faster decrease of the orbital order as compared to the spin order. The ordered state persists beyond $x = 0.5$ in our calculations. This robustness is an independent sign that doped holes form small polarons. Starting from the atomic limit, we have constructed the many-body wave function of a spin-orbital polaron bound to a defect. We have then established that the reduction of spin and orbital order obtained by unrestricted Hartree-Fock is consistent with that calculated with the help of the many-body spin-orbital polaron state. We note that, for a quantitative comparison with existing experimental data for the reduction of spin and orbital order and the insulator to metal transition [56,58], the inclusion of spin-orbit interaction and orbital polarization terms [91] is required.

In photoemission experiments of gapped systems, the position of the chemical potential μ is determined by defects. For the doped cubic vanadates, we find that μ lies in the center of the defect-states gap that forms inside the Mott-Hubbard gap. The defect potential $V_{\rm D}$, which basically confines doped holes to a cube formed by the V ions being the nearest neighbors of a charged defect, provides a measure of the upward shift of the in-gap defect states relative to the lower Hubbard band [67]. We found here that the distance of μ from the center of the lower Hubbard band scales linearly with V_D. Moreover, we found that this distance is basically unchanged by doping up to 50%, i.e., consistent with the photoemission study by Maiti and Sarma [69,70] for $La_{1-x}Ca_xVO_3$. We interpret this as a manifestation of small spin-orbital polaron physics. Furthermore, we have shown that the intensity of the $d^1 \rightarrow d^0$ satellite of the lower Hubbard band, that grows proportional to the doping concentration x, provides a direct fingerprint of the trapped spin-orbital polarons. The position in energy of this satellite relative to the lower Hubbard band and its width yields detailed information about the polarization of the SO polaron and the strength of random defect fields. For the $La_{1-x}Ca_xVO_3$ system, we found that the satellite is not well separated from the lower Hubbard band and thus has not been resolved in the existing PES experiments so far. Certainly, it would be very interesting to have high resolution photoemission or tunneling experiments carried out on this compound.

It is important to stress that our model, which includes simultaneously the defect Coulomb potential and the *e-e* interactions, is qualitatively different from the Coulomb glass

type of models not just because it contains orbital and spin degrees of freedom. The Coulomb glass model contains only a random distribution of defect state energies, thus the dipole (negative defect charge and positive bound hole) formation cannot take place. It is just this latter feature that makes an important difference between the results obtained by these two types of defect modeling (ours being definitely more realistic) and that leads to a weakening of the disorder with increasing *e*-*e* interactions. Instead, for Coulomb glass type of models, *e*-*e* interactions enhance localization [149].

Summarizing, we have demonstrated a systematic redistribution of the spectral weights with increasing doping by charged defects in Mott insulators using the example of $R_{1-x}Ca_xVO_3$. Even when doping is rather high, these systems remain insulating and the large Mott-Hubbard gap accommodate the spectral weight due to defect states, with the filled and unfilled defect states separated by a kinetic gap. We have also shown that the treatment of defects in strongly correlated materials with orbital degrees of freedom requires important extensions of the Hubbard-Anderson model. We designed a well motivated model for systems with orbital degrees of freedom to uncover the origin of the *satellite* structures that appear in doped systems and to explain the corresponding sum rules. In this way, the interpretation of photoemission and inverse photoemission experiments on Mott insulators doped with charged defects becomes possible. We have also explained why the spectral features, which arise from different excitation processes, can be energetically very close or overlap with one another, making them unresolvable in the experimental spectra.

Finally, one may ask whether there is any fundamental difference between doping into the vanadium perovskites and the cuprate high-T_c transition metal oxides. In both cases, the formal charge of the defects and the distance to the relevant electrons to the Cu or V ions, respectively, are similar. Nevertheless, in the cuprates, defects form shallow impurity states, whereas in the vanadates they are deep inside the gap. Our analysis shows that the additional orbital degree of freedom makes an important difference. The confinement of spin-orbital polarons in vanadates is *typically* on a single active bond, and thus is much stronger than the localization of spin polarons in cuprates. This also implies that the screening of defect potentials at low energy due to the defect states is weaker in vanadates, effectively leading to stronger binding of carriers and to a shift of the insulator-to-metal transition to much higher doping concentrations than in high-T_c materials.

ACKNOWLEDGMENTS

We thank B. Keimer and D. D. Sarma for insightful discussions. A.M.O. kindly acknowledges support by Narodowe Centrum Nauki (NCN, National Science Centre, Poland) under Project No. 2012/04/A/ST3/00331.

APPENDIX A: THE ALGORITHM TO DETERMINE STABLE CONFIGURATIONS WITH RANDOM DEFECTS

As we described in Sec. IV A, we present results obtained by averaging over 100 randomly chosen defect realizations. Any *random defect realization* is a configuration of defects defined by a set of randomly-chosen positions within the R lattice of doped $R_{1-x}Ca_xVO_3$ that host the Ca defects. Such positions, in terms of Cartesian coordinates, are obtained by subsequent calls to a pseudorandom number generator. No constraint is imposed (e.g., no minimal distance between the defects is required) except for the obvious hard-core constraint that any site is singly occupied, either by an R ion or by a Ca defect ion. The number of positions/defects in the set defines the degree of doping of the system x.

The employed Hartree-Fock self-consistency procedure is based on recursion: the values of all single-particle correlation functions appearing in the Hamiltonian are computed at each iteration after diagonalizing the Hamiltonian where the values computed at the previous iteration have been plugged in. The first iteration obviously requires externally-provided starting values (initialization), which are supplied on the basis of an educated guess. The recursion stops after a finite number of steps when all values in two subsequent iterations differ (actually the relative difference is used: $|x_{n-1} - x_n|/|x_{n-1}|$) at most by a chosen amount (i.e., 10^{-3}). In order to speed up the convergence and to avoid long cycles involving states with almost identical energies and slightly different values of the single-particle correlation functions characterizing them, the actual new values at each iteration are built as a linear combination of the old ones and the ones effectively obtained by diagonalizing the Hamiltonian. The proportion among the two components starts quite low in favor of the old values (0.1) and increases steadily with the iterations up to exclude the old values from the combination within 200 steps.

The size of the system ($N_a = 8 \times 8 \times 8$), the number of orbital and spin degrees of freedom per site ($6 = 3 \times 2$), and the number of random defect realizations to statistically average upon (100) make the numerical calculations very demanding and unavoidable to parallelize the code in order to keep the convergence for a set of Hamiltonian parameters within one day. In the finite system of N_a sites (atoms) considered here, we can change the defect concentration in steps of $1/512$. For instance, the low doping of $x = 1/64$ used in Fig. 25 corresponds to eight random defects. Each of these defects defines a cube of V ions around it and, at the very beginning, one hole is doped to each cube. *A priori,* we have no information about the ultimate doped holes' configuration for a given distribution of random defects, but the lowest energy configuration is self-consistently chosen to minimize the random fields acting on each hole.

The *procedure* developed to find this configuration is the following one: (i) we start from a *neutral* configuration (homogeneous doping of $1/8$) at each corner of any cube surrounding a defect at $\eta = 0$; (ii) increasing *e*-*e* interactions we reach $\eta = 1.0$ with full convergence at each value of η along the path in the parameter space for each starting configuration of random defects; (iii) starting from the final point of (ii) (and, therefore, exactly for all the same random defect configurations) we reach $\eta = 0$ with again full convergence at each value of η along this path. However, in (ii) and/or in (iii), if the convergence was lost along the way [for a value of $\eta \in (0.0 \rightarrow 1.0 \rightarrow 0.0)$], a new random configuration was used. Accordingly, if one looks carefully and, in particular, in the zoomed inset, one will see that also $\eta = 1.0$ is slightly different between the two panels (i.e., the two pathways) because of the last requirement.

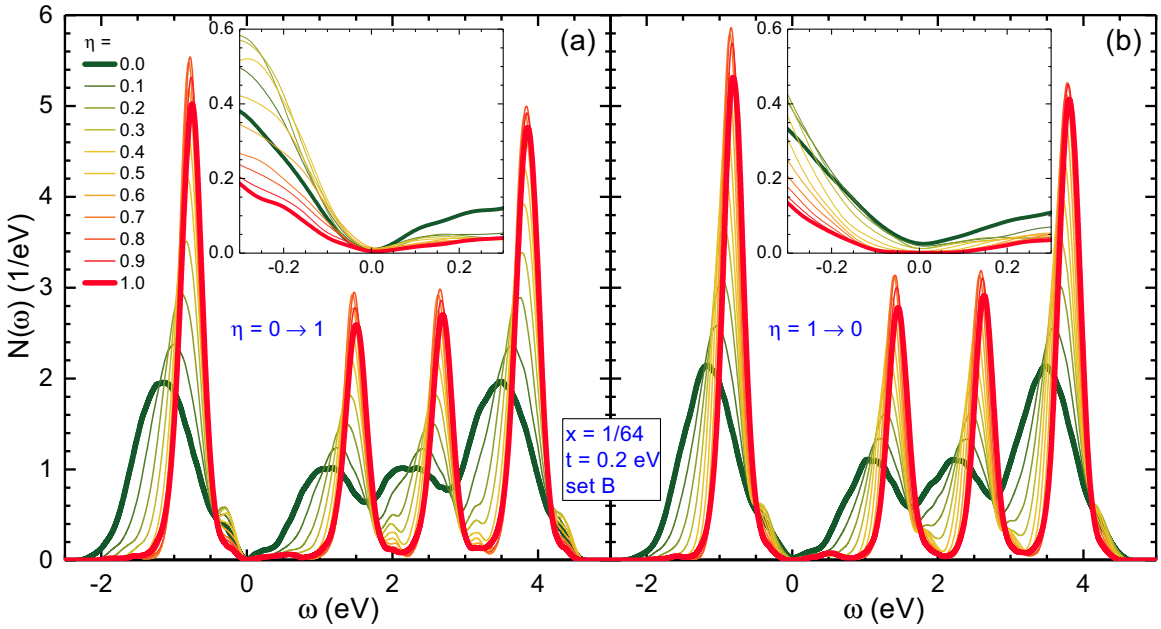

FIG. 25. t_{2g} DOS $N(\omega)$ as obtained for t_{2g} states from $M = 100$ random defect realizations for $t = 0.2$ eV at doping $x = 1/64$, and for (a) increasing value of e-e interaction (2.4) in steps of 0.1 from $\eta = 0$ (thick green line) to $\eta = 1.0$ (thick red line), and (b) decreasing value of e-e interaction (2.4) from $\eta = 1.0$ (thick red line) to $\eta = 0$ (thick green line). Insets show zooms of $N(\omega)$ near the Fermi energy at $\omega = 0$. Other parameters as in set B of Table I.

The rebooting procedure is necessary to stabilize the final results: when a set of values for a given Hamiltonian parameter is explored, if the convergence is not reached from the initial value of the set to the final value of it, we generated another random defect realization and reboot the search in order to get a smooth progression per each random defect realization. This rebooting procedure allows one to avoid taking into account random defect realizations with extremely weird relative positions of the defects that would hinder the convergence and that would be anyway discarded by *nature*.

The algorithm described above is unbiased, but rather involved. Therefore we present here a test of convergence carried out by performing the calculations at low doping, $x = 1/64$, and $t = 0.2$ eV in two ways: (i) starting with the case of absent e-e interactions ($\eta = 0$) and gradual switching on the screening interactions up to $\eta = 1.0$, and (ii) starting from the screened e-e interactions at $\eta = 1.0$ and reducing the screening down to $\eta = 0$. It is worth noting that the calculation performed starting from monopole interactions ($\eta = 0$) and reaching the state with screened e-e interactions ($\eta = 1.0$) leads to a physically very different state controlled effectively by dipolar interactions between defect centers, see Fig. 25(a). It is remarkable that the subsequent switching off of e-e interactions leads back to essentially the same initial state, see Fig. 25(b). For such a complex landscape, we are dealing with here, this is indeed a great result.

In fact, one finds very similar results independently of whether the e-e interactions are increased or reduced, see Figs. 25(a) and 25(b). In both cases, the system is an insulator, with distinct structures representing the LHB and UHB. If e-e interactions are absent ($\eta = 0$), the maxima corresponding to the LHB and the HS/LS excitations in the UHB are wide and the states that correspond to the excitations at sites occupied by holes cannot be resolved from these peaks. When the e-e interactions increase towards fully screened ones ($\eta = 1.0$), the defect states appear instead at the lower edges of both the LHB and the HS subband in the UHB. Both figures are remarkably similar even for the zoomed DOS near the Fermi energy, where a broader gap is visible at $\eta = 1.0$. This test confirms that the entire procedure, which includes the averaging over $M = 100$ random defect realizations, is reliable and gives well converged and reproducible results.

APPENDIX B: BOUND SPIN-ORBITAL POLARONS

In this Appendix, we shall analyze the reduction of the spin and orbital order parameters as functions of the doping x and of the kinetic energy parameter t in the frame of the spin-polaron theory. This strong coupling approach rests on the idea that, in the dilute limit, polaron-polaron interactions should be negligible due to the local nature of the polarons. This implies that the overall reduction of the order parameters can be determined in terms of the reduction induced by the polaron cloud of a single polaron, whose size scales with the kinetic energy parameter t. Accordingly, the overall reduction of the orders scales linearly with x, as in Eq. (7.3). Here, we shall first test up to which concentration x and to which kinetic energy parameter t, the independent polaron picture holds by inspecting the uHF results for the respective order parameters. Next, we shall derive the wave function for a spin polaron bound to a defect using the string basis introduced in Sec. VII. Finally, we shall compare the t dependence of the spin-polaron cloud with the order parameters calculated by the uHF method including the disorder. This will provide the basis for a qualitative and quantitative interpretation of the uHF

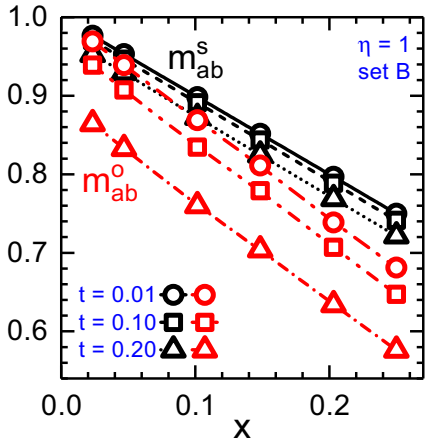

FIG. 26. Contributions from electrons in a/b orbitals to spin and orbital order parameters m^s_{ab} and m^o_{ab}, respectively, in the C-AF/G-AO ordered phase. The results from uHF theory are plotted as a function of doping x for different hopping parameters $t = 0.01, 0.10$, and 0.20 eV. Parameters as in Fig. 20.

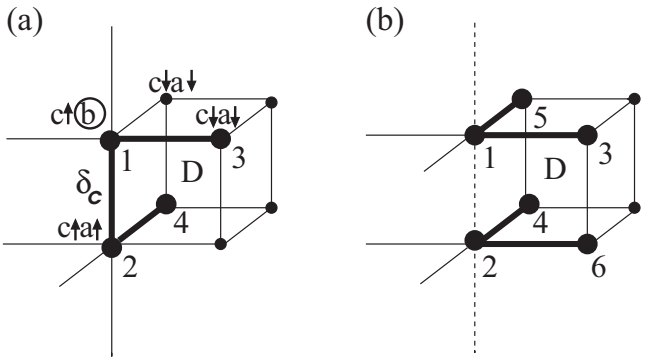

FIG. 27. String representation of the dominant contributions to the polaron wave function for a hole created by the annihilation of an occupied b orbital at site 1 close to the defect D. The hole delocalizes differently depending on the electron hopping in: (a) a or b orbitals and (b) c orbitals. The polarity δ_c of the active FM bond $\langle 1,2\rangle$ is mainly controlled by an interplay of the hopping amplitude t on that bond and the difference of random potentials between the sites 1 and 2.

results in the frame of the spin-orbital polaron theory emerging from the strong correlation picture.

Figure 26 displays the doping dependence of spin and orbital order parameters m^s_{ab} and m^o_{ab}, respectively, that are due to the electrons in a and b orbitals. The figure highlights an approximate linearity in x of the uHF results up to high doping concentrations. This is a clear evidence that the small-polaron picture applies for the values of t considered in Fig. 26 and suggests that the interactions among polarons are of minor importance and, therefore, negligible in first approximation. Moreover, the uHF results show that the decrease of the spin moments m^s_{ab} with t is much slower as compared to that of the orbital-order parameter m^o_{ab}. This confirms that the spin order in doped systems is more robust [55] as the FM polarization along the active bonds is not affected when the orbital order is locally disturbed. Nevertheless, in Fig. 26, one notices small nonlinearities in m^s_{ab} at small values of x, which we attribute to the random far-defect potentials.

The spatial symmetry of the polaron depends on the magnetic and the orbital order. For instance, a hole in the AF CuO_2 planes of high-Tc superconductors takes the form of a Zhang-Rice singlet, that is, a combination of the Cu $d_{x^2-y^2}$ orbital and of a d-wave admixture of the $2p$ states from the four oxygen neighbors. The symmetry of the wave function is C_2 relative to the c-axis (but C_4 for the probability distribution). A spin polaron in the C-AF/G-AO state has a C_2 symmetry for both the wave function and its probability distribution. Since these SO polarons are bound to the defect, their symmetry is further reduced due to the strong Coulomb attraction of the charged defect.

Figure 27 shows the most important string states that contribute to the bound polaron wave function for a hole created at the V site 1 by annihilation of a b electron with spin up in the undoped ground state $|\Phi_0\rangle$:

$$|\Phi_0\rangle = |c\uparrow,b\uparrow;c\uparrow,a\uparrow;c\downarrow,a\downarrow;c\downarrow,b\downarrow\rangle. \tag{B1}$$

The vacuum state $|\Phi_0\rangle$ indicates the occupied orbitals and spin orientations consistent with the C-AF/G-AO order for the ions sited at sites 1, 2, 3, and 4 [see Fig. 27(a)]. Due to the strong attraction of the defect D, the relevant string states 1, 2, 3, and 4 are all on the defect cube. Moreover, the selected strings reflect the constraints due to the spin- and orbital-order and the flavor conserving constrained hopping processes. Figures 27(a) and 27(b) distinguish strings for electrons in a/b and c orbitals, respectively. We shall discuss here only the contributions that stem from a and b orbitals that have the largest effect on the order parameters. The relevant string states are

$$\begin{aligned}
|\Phi_1\rangle &= |c\uparrow,0;c\uparrow,a\uparrow;c\downarrow,a\downarrow;c\downarrow,b\downarrow\rangle,\\
|\Phi_2\rangle &= |c\uparrow,a\uparrow;c\uparrow,0;c\downarrow,a\downarrow;c\downarrow,b\downarrow\rangle,\\
|\Phi_3\rangle &= |c\uparrow,a\downarrow;c\uparrow,a\uparrow;c\downarrow,0;c\downarrow,b\downarrow\rangle,\\
|\Phi_4\rangle &= |c\uparrow,a\uparrow;c\uparrow,b\downarrow;c\downarrow,a\downarrow;c\downarrow,0\rangle.
\end{aligned} \tag{B2}$$

Here, $|\Phi_1\rangle$ is the original configuration arising from the annihilation of an up-spin electron in a b orbital at the V-site 1. In state $|\Phi_2\rangle$, the a electron has moved along the FM bond from site 2 to site 1. This interchange results in an orbital excitation at site 1. Since the Jahn-Teller energy is small, the kinetic energy will mix these two states. However, the active bond 1-2 is further controlled by the random far-defect potentials. Therefore it is useful to characterize the distribution of electrons (or holes) on the active bond by the polarity parameter δ_c:

$$|\Psi_1(\delta_c)\rangle = \sqrt{1-\delta_c}|\Phi'_1\rangle + \sqrt{\delta_c}|\Phi'_2\rangle, \tag{B3}$$

where for $n = 1$ and 2:

$$|\Phi'_n\rangle = \frac{|\Phi_n\rangle + \frac{t}{e_0}|\Phi_{n+2}\rangle}{\sqrt{1+\left(\frac{t}{e_0}\right)^2}}. \tag{B4}$$

These states contain admixtures from strings 1 and 2, and 3 and 4, respectively, which involve low-spin excitations with excitation energy $e_0 = J_H$. According to Eq. (B3), the polaron state for $\delta_c = 0$ corresponds to a hole at site 1 and for $\delta_c = 1$ to a hole at site 2, in combination with an orbital excitation at site 1. Increasing the kinetic energy parameter t will eventually push δ_c towards $1/2$.

By means of the spin-polaron wave function $|\Psi_1(\delta_c)\rangle$, we can evaluate the reduction of the spin and orbital order due to a single polaron [see Eq. (7.4)]:

$$m_{ab}^{sP} \cong 1 + \frac{2(t/e_0)^2}{1+(t/e_0)^2},$$
$$m_{ab}^{oP} \cong 1 + 2\delta_c + \frac{2(t/e_0)^2}{1+(t/e_0)^2}. \quad \text{(B5)}$$

We note that the potential of the random far defects will modify the excitation energy e_0. Moreover, the polarity parameter δ_c too is determined by the interplay of the kinetic energy parameter t and the same far-defect random potentials.

The total reduction of spin- and orbital-order associated with a/b electrons is then [Eq. (7.3)]:

$$m_{ab}^{s} \cong 1 - x\left[1 + \frac{2(t/e_0)^2}{1+(t/e_0)^2}\right],$$
$$m_{ab}^{o} \cong 1 - x\left[1 + 2\delta_c + \frac{2(t/e_0)^2}{1+(t/e_0)^2}\right]. \quad \text{(B6)}$$

In Fig. 28, we report a least-square fit of the uHF results for the spin-order parameter m_{ab}^s to the above polaron expression with a single variational parameter, namely, the activation energy e_0. Since the uHF results represent a statistical average over many defect realizations, the resulting activation energy $e_0(x)$ characterizes a *typical* spin-orbital polaron bound state. It is worth noting that m_{ab}^s does not depend on the active bond parameter δ_c. This is distinct from the orbital order since the motion of the hole on the active bond creates an orbital defect yet no spin defect (see discussion in Sec. VII).

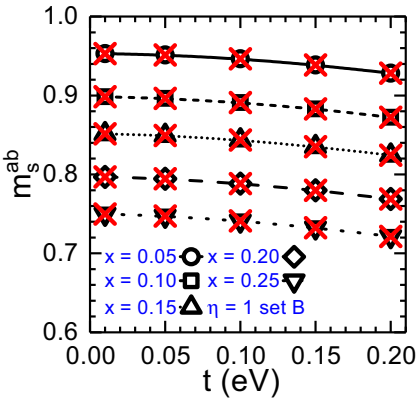

FIG. 28. Contributions from electrons in a/b orbitals to spin-order parameter m_{ab}^s as a function of t as calculated by the uHF method (black symbols). Parameters as in Fig. 20. A fit of m_{ab}^s to the polaron theory Eq. (B6) for doping concentrations $x = 5, 10, 15, 20$ and 25% is marked by red crosses.

Our results show that even up to a doping concentration of $x = 25\%$, the reduction of both order parameters is approximately linear, this holds true even when $t = 0.2$ eV, i.e., for a typical value of the kinetic energy parameter for the vanadate compounds. It is worth noting that the uHF is able to describe also the interaction between polarons, which appears however irrelevant in the data range shown in Fig. 28. That the independent polaron ansatz works so well for such huge doping concentrations may appear really surprising. On the other hand, one may have expected this given the extreme localization of the defect states we have inferred by exploring the inverse participation number in Sec. VI.

[1] M. Imada, A. Fujimori, and Y. Tokura, Metal-Insulator Transitions, Rev. Mod. Phys. **70**, 1039 (1998).

[2] H. Y. Hwang, Y. Iwasa, M. Kawasaki, B. Keimer, N. Nagaosa, and Y. Tokura, Emergent phenomena at oxide interfaces, Nat. Mater. **11**, 103 (2012).

[3] L. Balents, Spin liquids in frustrated magnets, Nature (London) **464**, 199 (2010).

[4] S. Sachdev and B. Keimer, Quantum criticality, Phys. Today **64**(2), 29 (2011).

[5] L. Savary and L. Balents, Quantum spin liquids: A review, Rep. Prog. Phys. **80**, 016502 (2017).

[6] Y. Zhou, K. Kanoda, and T.-K. Ng, Quantum spin liquid states, Rev. Mod. Phys. **89**, 025003 (2017).

[7] P. A. Lee, N. Nagaosa, and X.-G. Wen, Doping a Mott insulator: Physics of high-temperature superconductivity, Rev. Mod. Phys. **78**, 17 (2006).

[8] H. Alloul, J. Bobroff, M. Gabay, and P. J. Hirschfeld, Defects in correlated metals and superconductors, Rev. Mod. Phys. **81**, 45 (2009).

[9] E. Berg, E. Fradkin, S. A. Kivelson, and J. M. Tranquada, Striped superconductors: How spin, charge and superconducting orders intertwine in the cuprates, New J. Phys. **11**, 115004 (2011).

[10] A. Avella, Composite operator method analysis of the underdoped cuprates puzzle, Adv. Condens. Matter Phys. **2014**, 515698 (2014).

[11] B. Ellman, H. M. Jaeger, D. P. Katz, T. F. Rosenbaum, A. S. Cooper, and G. P. Espinosa, Transport studies of $La_{2-x}Sr_xCuO_4$ near the insulator-metal-superconductor transition, Phys. Rev. B **39**, 9012 (1989).

[12] G. Khaliullin and P. Horsch, Doping dependence of long-range magnetic order in the t-J model, Phys. Rev. B **47**, 463 (1993).

[13] M. A. Kastner, R. J. Birgeneau, G. Shirane, and Y. Endoh, Magnetic, transport, and optical properties of monolayer copper oxides, Rev. Mod. Phys. **70**, 897 (1998).

[14] K. I. Kugel and D. I. Khomskii, The Jahn-Teller effect and magnetism: Transition metal compounds, Sov. Phys. Usp. **25**, 231 (1982).

[15] Y. Tokura and N. Nagaosa, Orbital physics in transition-metal oxides, Science **288**, 462 (2000).

[16] A. M. Oleś, G. Khaliullin, P. Horsch, and L. F. Feiner, Fingerprints of spin-orbital physics in cubic Mott insulators: Magnetic exchange interactions and optical spectral weights, Phys. Rev. B **72**, 214431 (2005).

[17] G. Khaliullin, Orbital order and fluctuations in Mott insulators, Prog. Theor. Phys. Suppl. **160**, 155 (2005).

[18] P. Horsch, Orbital Physics in Transition Metal Oxides: Magnetism and Optics, in *Handbook of Magnetism and Advanced Magnetic Materials*, edited by H. Kronmueller and S. Parkin (Wiley, New York, 2007).

[19] A. M. Oleś, Fingerprints of spin-orbital entanglement in transition metal oxides, J. Phys.: Condens. Matter **24**, 313201 (2012).

[20] R. Kilian and G. Khaliullin, Orbital polarons in the metal-insulator transition of manganites, Phys. Rev. B **60**, 13458 (1999).

[21] L. F. Feiner and A. M. Oleś, Electronic origin of magnetic and orbital ordering in insulating $LaMnO_3$, Phys. Rev. B **59**, 3295 (1999).

[22] A. Weisse and H. Fehske, Microscopic modelling of doped manganites, New J. Phys. **6**, 158 (2004).

[23] M. Daghofer, A. M. Oleś, and W. von der Linden, Orbital polarons versus itinerant e_g electrons in doped manganites, Phys. Rev. B **70**, 184430 (2004).

[24] J. Geck, P. Wochner, S. Kiele, R. Klingeler, P. Reutler, A. Revcolevschi, and B. Buchner, Orbital Polaron Lattice Formation in Lightly Doped $La_{1-x}Sr_xMnO_3$, Phys. Rev. Lett. **95**, 236401 (2005).

[25] A. M. Oleś and G. Khaliullin, Dimensional crossover and the magnetic transition in electron doped manganites, Phys. Rev. B **84**, 214414 (2011).

[26] M. Snamina and A. M. Oleś, Spin-orbital order in the undoped manganite $LaMnO_3$ at finite temperature, Phys. Rev. B **94**, 214426 (2016); Spin-orbital model of stoichiometric $LaMnO_3$ with tetragonal distortions, **97**, 104417 (2018).

[27] E. Dagotto, T. Hotta, and A. Moreo, Colossal magnetoresistant materials: The key role of phase separation, Phys. Rep. **344**, 1 (2001).

[28] E. Dagotto, Open questions in CMR manganites, relevance of clustered states and analogies with other compounds including the cuprates, New J. Phys. **7**, 67 (2005).

[29] Y. Tokura, Critical features of colossal magnetoresistive manganites, Rep. Prog. Phys. **69**, 797 (2006).

[30] M. De Raychaudhury, E. Pavarini, and O. K. Andersen, Orbital Fluctuations in the Different Phases of $LaVO_3$ and YVO_3, Phys. Rev. Lett. **99**, 126402 (2007).

[31] G. Khaliullin and S. Maekawa, Orbital Liquid in Three-Dimensional Mott Insulator: $LaTiO_3$, Phys. Rev. Lett. **85**, 3950 (2000).

[32] M. Mochizuki, Spin and orbital states and their phase transitions of the perovskite-type Ti oxides: Weak coupling approach, J. Phys. Soc. Jpn. **71**, 2039 (2002).

[33] G. Khaliullin and S. Okamoto, Theory of orbital state and spin interactions in ferromagnetic titanates, Phys. Rev. B **68**, 205109 (2003).

[34] S. Ishihara, Orbital wave and its observation in orbital-ordered titanates and vanadates, Phys. Rev. B **69**, 075118 (2004).

[35] J.-G. Cheng, Y. Sui, J.-S. Zhou, J. B. Goodenough, and W. H. Su, Transition from Orbital Liquid to Jahn-Teller Insulator in Orthorhombic Perovskites $R TiO_3$, Phys. Rev. Lett. **101**, 087205 (2008).

[36] C. Ulrich, G. Khaliullin, M. Guennou, H. Roth, T. Lorenz, and B. Keimer, Spin-Orbital Excitation Continuum and Anomalous Electron-Phonon Interaction in the Mott Insulator $LaTiO_3$, Phys. Rev. Lett. **115**, 156403 (2015).

[37] J. F. Schooley, W. R. Hosler, and M. L. Cohen, Superconductivity in Semiconducting $SrTiO_3$, Phys. Rev. Lett. **12**, 474 (1964).

[38] Y. Kozuka, M. Kim, C. Bell, B. G. Kim, Y. Hikita, and H. Y. Hwang, Two-dimensional normal-state quantum oscillations in a superconducting heterostructure, Nature (London) **462**, 487 (2009).

[39] L. Li, C. Richter, J. Mannhart, and R. C. Ashoori, Coexistence of magnetic order and two-dimensional superconductivity at $LaAlO_3/SrTiO_3$ interfaces, Nat. Phys. **7**, 762 (2011).

[40] M. Gabay and J. M. Triscone, Hund rules with a twist, Nat. Phys. **9**, 610 (2013).

[41] Y. Ren, T. T. M. Palstra, D. I. Khomskii, E. Pellegrin, A. A. Nugroho, A. A. Menovsky, and G. A. Sawatzky, Temperature-induced magnetization reversal in a YVO_3 single crystal, Nature (London) **396**, 441 (1998).

[42] Y. Ren, T. T. M. Palstra, D. I. Khomskii, A. A. Nugroho, A. A. Menovsky, and G. A. Sawatzky, Magnetic properties of YVO_3 single crystals, Phys. Rev. B **62**, 6577 (2000).

[43] G. Khaliullin, P. Horsch, and A. M. Oleś, Spin Order due to Orbital Fluctuations: Cubic Vanadates, Phys. Rev. Lett. **86**, 3879 (2001).

[44] P. Horsch, G. Khaliullin, and A. M. Oleś, Dimerization versus Orbital-Moment Ordering in a Mott Insulator YVO_3, Phys. Rev. Lett. **91**, 257203 (2003).

[45] C. Ulrich, G. Khaliullin, J. Sirker, M. Reehuis, M. Ohl, S. Miyasaka, Y. Tokura, and B. Keimer, Magnetic Neutron Scattering Study of YVO_3: Evidence for an Orbital Peierls State, Phys. Rev. Lett. **91**, 257202 (2003).

[46] J. Sirker and G. Khaliullin, Entropy driven dimerization in a one-dimensional spin-orbital model, Phys. Rev. B **67**, 100408 (2003).

[47] J. Sirker, A. Herzog, A. M. Oleś, and P. Horsch, Thermally Activated Peierls Dimerization in Ferromagnetic Spin Chains, Phys. Rev. Lett. **101**, 157204 (2008).

[48] S. Miyasaka, Y. Okimoto, M. Iwama, and Y. Tokura, Spin-orbital phase diagram of perovskite-type RVO_3 (R=rare-earth ion or Y), Phys. Rev. B **68**, 100406 (2003).

[49] S. Miyasaka, J. Fujioka, M. Iwama, Y. Okimoto, and Y. Tokura, Raman study of spin and orbital order and excitations in perovskite-type RVO_3 (R = La, Nd, and Y), Phys. Rev. B **73**, 224436 (2006).

[50] J. Fujioka, T. Yasue, S. Miyasaka, Y. Yamasaki, T. Arima, H. Sagayama, T. Inami, K. Ishii, and Y. Tokura, Critical competition between two distinct orbital-spin ordered states in perovskite vanadates, Phys. Rev. B **82**, 144425 (2010).

[51] S. Miyasaka, T. Yasue, J. Fujioka, Y. Yamasaki, Y. Okimoto, R. Kumai, T. Arima, and Y. Tokura, Magnetic Field Switching between the Two Orbital-Ordered States in $DyVO_3$, Phys. Rev. Lett. **99**, 217201 (2007).

[52] M. H. Sage, G. R. Blake, C. Marquina, and T. T. M. Palstra, Competing orbital ordering in RVO_3 compounds: High-resolution x-ray diffraction and thermal expansion, Phys. Rev. B **76**, 195102 (2007).

[53] M. Reehuis, C. Ulrich, K. Prokeš, S. Mat'aš, J. Fujioka, S. Miyasaka, Y. Tokura, and B. Keimer, Structural and magnetic phase transitions of the orthovanadates RVO_3 (R = Dy, Ho, Er) as seen via neutron diffraction, Phys. Rev. B **83**, 064404 (2011).

[54] I. Lindfors-Vrejoiu, L. Jin, C. Himcinschi, J. Engelmayer, F. Hensling, C.-L. Jia, R. Waser, R. Dittmann, and P. H. M. van Loosdrecht, Structure and orbital ordering of ultrathin $LaVO_3$ probed by atomic resolution electron microscopy and Raman

spectroscopy, Phys. Status Solidi–Rapid Res. Lett. **11**, 1600350 (2017).

[55] S. Miyasaka, T. Okuda, and Y. Tokura, Critical Behavior of Metal-Insulator Transition in $La_{1-x}Sr_xVO_3$, Phys. Rev. Lett. **85**, 5388 (2000).

[56] J. Fujioka, S. Miyasaka, and Y. Tokura, Orbital disordering and the metal-insulator transition with hole doping in perovskite-type vanadium oxides, Phys. Rev. B **72**, 024460 (2005).

[57] J. Fujioka, S. Miyasaka, and Y. Tokura, Doping variation of anisotropic charge and orbital dynamics in $Y_{1-x}Ca_xVO_3$: Comparison with $La_{1-x}Sr_xVO_3$, Phys. Rev. B **77**, 144402 (2008).

[58] M. Reehuis, C. Ulrich, P. M. Abdala, P. Pattison, G. Khaliullin, J. Fujioka, S. Miyasaka, Y. Tokura, and B. Keimer, Spin and orbital disordering by hole doping in $Pr_{1-x}Ca_xVO_3$, Phys. Rev. B **94**, 104436 (2016).

[59] M. Daghofer, P. Horsch, and G. Khaliullin, Magnetic Properties of Spin-Orbital Polarons in Lightly Doped Cobaltates, Phys. Rev. Lett. **96**, 216404 (2006).

[60] K. Wohlfeld, A. M. Oleś, and P. Horsch, Orbitally induced string formation in the spin-orbital polarons, Phys. Rev. B **79**, 224433 (2009).

[61] M. Berciu, Challenging a Hole to Move through an Ordered Insulator, Physics **2**, 55 (2009).

[62] K. Bieniasz, M. Berciu, and A. M. Oleś, Orbiton-magnon interplay in the spin-orbital polarons of $KCuF_3$ and $LaMnO_3$, Phys. Rev. B **95**, 235153 (2017).

[63] A. Avella, A. M. Oleś, and P. Horsch, Defects, Disorder, and Strong Electron Correlations in Orbital Degenerate, Doped Mott Insulators, Phys. Rev. Lett. **115**, 206403 (2015).

[64] C. Y. Chen, R. J. Birgeneau, M. A. Kastner, N. W. Preyer, and T. Thio, Frequency and magnetic-field dependence of the dielectric constant and conductivity of La_2CuO_{4+y}, Phys. Rev. B **43**, 392 (1991).

[65] W. Chen, G. Khaliullin, and O. P. Sushkov, Coulomb disorder effects on angle-resolved photoemission and nuclear quadrupole resonance spectra in cuprates, Phys. Rev. B **80**, 094519 (2009).

[66] P. Horsch, A. M. Oleś, L. F. Feiner, and G. Khaliullin, Evolution of Spin-Orbital-Lattice Coupling in the RVO_3 Perovskites, Phys. Rev. Lett. **100**, 167205 (2008).

[67] P. Horsch and A. M. Oleś, Defect states and spin-orbital physics in doped vanadates $Y_{1-x}Ca_xVO_3$, Phys. Rev. B **84**, 064429 (2011).

[68] D. Bizen, H. Nakao, K. Iwasa, Y. Murakami, T. Osakabe, J. Fujioka, T. Yasue, S. Miyasaka, and Y. Tokura, Magnetic phase diagrams of YVO_3 and $TbVO_3$ under high pressure, J. Phys. Soc. Jpn. **81**, 024715 (2012).

[69] K. Maiti, P. Mahadevan, and D. D. Sarma, Evolution of Spectral Function in a Doped Mott Insulator: Surface vs Bulk Contributions, Phys. Rev. Lett. **80**, 2885 (1998).

[70] K. Maiti and D. D. Sarma, Spectroscopic investigations of the electronic structure and metal-insulator transitions in a Mott-Hubbard system $La_{1-x}Ca_xVO_3$, Phys. Rev. B **61**, 2525 (2000).

[71] H. F. Pen, M. Abbate, A. Fujimori, Y. Tokura, H. Eisaki, S. Uchida, and G. A. Sawatzky, Electronic structure of $Y_{1-x}Ca_xVO_3$ studied by high-energy spectroscopies, Phys. Rev. B **59**, 7422 (1999).

[72] V. F. Gantmakher, *Electrons and Disorder in Solids* (Clarendon Press, Oxford, 2005).

[73] *Theory of Defects in Semiconductors*, edited by D. A. Drabold and S. K. Estreicher (Springer, Berlin, Heidelberg, 2007).

[74] P. W. Anderson, Absence of diffusion in certain random lattices, Phys. Rev. **109**, 1492 (1958).

[75] P. A. Lee and T. V. Ramakrishnan, Disordered electronic systems, Rev. Mod. Phys. **57**, 287 (1985).

[76] B. L. Altshuler and A. A. Aronov, Zero bias anomaly in tunnel resistance and electron-electron interaction, Solid State Commun. **30**, 115 (1979).

[77] M. Pollack, Effect of carrier-carrier interactions on some transport properties in disordered semiconductors, Discuss. Faraday Soc. **50**, 20 (1970).

[78] A. L. Efros and B. I. Shklovskii, Coulomb gap and low temperature conductivity of disordered systems, J. Phys. C **8**, L49 (1975).

[79] A. L. Efros, Coulomb gap in disordered systems, J. Phys. C **9**, 2021 (1976).

[80] A. L. Efros, B. Skinner, and B. I. Shklovskii, Coulomb gap in the one-particle density of states in three-dimensional systems with localized electrons, Phys. Rev. B **84**, 064204 (2011).

[81] H. Shinaoka and M. Imada, Single-particle excitations under coexisting electron correlation and disorder: A numerical study of the Anderson-Hubbard model, J. Phys. Soc. Jpn. **78**, 094708 (2009).

[82] H. Shinaoka and M. Imada, Theory of electron transport near Anderson-Mott transition, J. Phys. Soc. Jpn. **79**, 113703 (2010).

[83] F. Epperlein, M. Schreiber, and T. Vojta, Quantum Coulomb glass within a Hartree-Fock approximation, Phys. Rev. B **56**, 5890 (1997).

[84] Y. Song, S. Bulut, R. Wortis, and W. A. Atkinson, Effects of strong correlations on the disorder-induced zero-bias anomaly in the extended Anderson–Hubbard model, J. Phys.: Condens. Matter **21**, 385601 (2009).

[85] T. Mizokawa, D. I. Khomskii, and G. A. Sawatzky, Charge and orbital ordering in underdoped $La_{1-x}Sr_xMnO_3$, Phys. Rev. B **61**, R3776 (2000).

[86] C. Barreteau, R. Guirado-Lopez, D. Spanjaard, M. C. Desjonquères, and A. M. Oleś, spd tight-binding model of magnetism in transition metals: Application to Rh and Pd clusters and slabs, Phys. Rev. B **61**, 7781 (2000).

[87] T. Hotta, S. Yunoki, M. Mayr, and E. Dagotto, *A*-type antiferromagnetic and *C*-type orbital-ordered states in $LaMnO_3$ using cooperative Jahn-Teller phonons, Phys. Rev. B **60**, R15009(R) (1999); Q. Luo, K. Foyevtsova, G. D. Samolyuk, F. Reboredo, and E. Dagotto, Magnetic states of the five-orbital Hubbard model for one-dimensional iron-based superconductors, *ibid.* **90**, 035128 (2014); G. Liu, N. Kaushal, S. Li, C. B. Bishop, Y. Wang, S. Johnston, G. Alvarez, A. Moreo, and E. Dagotto, Orbital-selective Mott phases of a one-dimensional three-orbital Hubbard model studied using computational techniques, Phys. Rev. E **93**, 063313 (2016).

[88] V. I. Solovyev, Combining DFT and many-body methods to understand correlated materials, J. Phys.: Condens. Matter **20**, 293201 (2008).

[89] J. Carrasco, F. Illas, N. Lopez, E. A. Kotomin, Y. F. Zhukovskii, R. A. Evarestov, Y. A. Mastrikov, S. Piskunov, and J. Maier, First-principles calculations of the atomic and electronic structure of F centers in the bulk and on the (001) surface of $SrTiO_3$, Phys. Rev. B **73**, 064106 (2006).

[90] N. Pavlenko, T. Kopp, E. Y. Tsymbal, J. Mannhart, and G. A. Sawatzky, Oxygen vacancies at titanate interfaces: Two-dimensional magnetism and orbital reconstruction, Phys. Rev. B **86**, 064431 (2012).

[91] A. Avella, P. Horsch, and A. M. Oleś, Defect states and excitations in a Mott insulator with orbital degrees of freedom: Mott-Hubbard gap versus optical and transport gaps in doped systems, Phys. Rev. B **87**, 045132 (2013).

[92] T. Mizokawa and A. Fujimori, Unrestricted Hartree-Fock study of transition-metal oxides: Spin and orbital ordering in perovskite-type lattice, Phys. Rev. B **51**, 12880 (1995).

[93] T. Mizokawa and A. Fujimori, Hartree-Fock study of charge-ordered states in $La_{2-x}Sr_xCuO_4$ and $La_{2-x}Sr_xNiO_4$, Phys. Rev. B **56**, 11920 (1997).

[94] H. Weng and K. Terakura, Phase diagram of $LaVO_3$ under epitaxial strain: Implications for thin films grown on $SrTiO_3$ and $LaAlO_3$ substrates, Phys. Rev. B **82**, 115105 (2010).

[95] V. I. Solovyev, Long-range magnetic interactions induced by the lattice distortions and the origin of the E-type antiferromagnetic phase in the undoped orthorhombic manganites, J. Phys. Soc. Jpn. **78**, 054710 (2009).

[96] K. Kubo and P. Thalmeier, Multiorbital effects on antiferromagnetism in Fe pnictides, J. Phys. Soc. Jpn. **78**, 083704 (2009).

[97] T. Schickling, F. Gebhard, and J. Bünemann, Antiferromagnetic Order in Multiband Hubbard Models for Iron Pnictides, Phys. Rev. Lett. **106**, 146402 (2011).

[98] Q. Luo, A. Nicholson, J. Rincón, S. Liang, J. Riera, G. Alvarez, L. Wang, W. Ku, G. D. Samolyuk, A. Moreo, and E. Dagotto, Magnetic states of the two-leg-ladder alkali metal iron selenides AFe_2Se_3, Phys. Rev. B **87**, 024404 (2013).

[99] Q. Luo and E. Dagotto, Magnetic phase diagram of a five-orbital Hubbard model in the real-space Hartree-Fock approximation varying the electronic density, Phys. Rev. B **89**, 045115 (2014).

[100] R. J. Bell and P. Dean, Atomic vibrations in vitreous silica, Discuss. Faraday Soc. **50**, 55 (1970).

[101] D. J. Thouless, Electrons in disordered systems and the theory of localization, Phys. Rep. **13**, 93 (1974).

[102] F. Wegner, Inverse participation ratio in $2+\varepsilon$ dimensions, Z. Phys. B **36**, 209 (1980).

[103] H. C. Nguyen and J. B. Goodenough, Localized-itinerant electronic transition in the perovskite system $La_{1-x}Ca_xVO_3$, Phys. Rev. B **52**, 8776 (1995).

[104] A. Damascelli, Z. Hussain, and Z.-X. Shen, Angle-resolved photoemission studies of the cuprate superconductors, Rev. Mod. Phys. **75**, 473 (2003).

[105] R. Comin and A. Damascelli, Resonant X-Ray scattering studies of charge order in cuprates, Annu. Rev. Condens. Matter Phys. **7**, 369 (2016).

[106] G. Khaliullin, P. Horsch, and A. M. Oleś, Theory of optical spectral weights in Mott insulators with orbital degrees of freedom, Phys. Rev. B **70**, 195103 (2004).

[107] A. A. Tsvetkov, F. P. Mena, P. H. M. van Loosdrecht, D. van der Marel, Y. Ren, A. A. Nugroho, A. A. Menovsky, I. S. Elfimov, and G. A. Sawatzky, Structural, electronic, and magneto-optical properties of YVO_3, Phys. Rev. B **69**, 075110 (2004).

[108] A. B. Harris, T. Yildirim, A. Aharony, O. Entin-Wohlman, and I. Y. Korenblit, Unusual Symmetries in the Kugel-Khomskii Hamiltonian, Phys. Rev. Lett. **91**, 087206 (2003).

[109] M. Daghofer, K. Wohlfeld, A. M. Oleś, E. Arrigoni, and P. Horsch, Absence of Hole Confinement in Transition-Metal Oxides with Orbital Degeneracy, Phys. Rev. Lett. **100**, 066403 (2008).

[110] Y. Li, Exact results for itinerant ferromagnetism in a t_{2g}-orbital system on cubic and square lattices, Phys. Rev. B **91**, 115122 (2015).

[111] A. M. Oleś, Antiferromagnetism and correlation of electrons in transition metals, Phys. Rev. B **28**, 327 (1983).

[112] M. Daghofer, A. Nicholson, A. Moreo, and E. Dagotto, Three orbital model for the iron-based superconductors, Phys. Rev. B **81**, 014511 (2010).

[113] M. Mayr and P. Horsch, Domain-wall excitations and optical conductivity in one-dimensional Wigner lattices, Phys. Rev. B **73**, 195103 (2006).

[114] Y. Matiks, P. Horsch, R. K. Kremer, B. Keimer, and A. V. Boris, Exciton Doublet in the Mott-Hubbard Insulator $LiCuVO_4$ Identified by Spectral Ellipsometry, Phys. Rev. Lett. **103**, 187401 (2009).

[115] W. F. Brinkman and T. M. Rice, Single-particle excitations in magnetic insulators, Phys. Rev. B **2**, 1324 (1970).

[116] H. Eskes, M. B. J. Meinders, and G. A. Sawatzky, Anomalous Transfer of Spectral Weight in Doped Strongly Correlated Systems, Phys. Rev. Lett. **67**, 1035 (1991).

[117] M. B. J. Meinders, H. Eskes, and G. A. Sawatzky, Spectral-weight transfer: Breakdown of low-energy-scale sum rules in correlated systems, Phys. Rev. B **48**, 3916 (1993).

[118] A. Fujimori, I. Hase, H. Namatame, Y. Fujishima, Y. Tokura, H. Eisaki, S. Uchida, K. Takegahara, and F. M. F. de Groot, Evolution of the Spectral function in Mott-Hubbard Systems with d^1 Configuration, Phys. Rev. Lett. **69**, 1796 (1992).

[119] E. Dagotto, A. Moreo, F. Ortolani, D. Poilblanc, and J. Riera, Static and dynamical properties of doped Hubbard clusters, Phys. Rev. B **45**, 10741 (1992).

[120] H. Eskes and A. M. Oleś, Two Hubbard Bands: Weight Transfer in Optical and One-Particle Spectra, Phys. Rev. Lett. **73**, 1279 (1994).

[121] H. Eskes, A. M. Oleś, M. B. J. Meinders, and W. Stephan, Spectral properties of the Hubbard bands, Phys. Rev. B **50**, 17980 (1994).

[122] L. de'Medici, A. Georges, and S. Biermann, Orbital-selective Mott transition in multiband systems: Slave-spin representation and dynamical mean-field theory, Phys. Rev. B **72**, 205124 (2005).

[123] C. Chen, Spectral Function Evolution in a Muliband d-Electron Model: Combined Single-Particle and Many-Body Effects, Phys. Rev. Lett. **73**, 1982 (1994).

[124] L. Vaugier, H. Jiang, and S. Biermann, Hubbard U and Hund exchange J in transition metal oxides: Screening versus localization trends from constrained random phase approximation, Phys. Rev. B **86**, 165105 (2012).

[125] D. Vollhardt, Characteristic Crossing Points in Specific Heat Curves of Correlated Systems, Phys. Rev. Lett. **78**, 1307 (1997).

[126] M. Greger, M. Kollar, and D. Vollhardt, Isosbestic points: How a narrow crossing region of curves determines their leading parameter dependence, Phys. Rev. B **87**, 195140 (2013).

[127] T. Guhr, A. Muller-Groeling, and H. A. Weidenmuller, Random-matrix theories in quantum physics: Common concepts, Phys. Rep. **299**, 190 (1998).

[128] Y. Ono, T. Ohtsuki, and B. Kramer, Inverse participation number and fractal dimensionality of electronic states in a two dimensional system in strong perpendicular magnetic field, J. Phys. Soc. Jpn. **58**, 1705 (1989).

[129] F. Evers and A. D. Mirlin, Anderson transitions, Rev. Mod. Phys. **80**, 1355 (2008).

[130] G. Misguich, V. Pasquier, and J.-M. Luck, Inverse participation ratios in the XXZ spin chain, Phys. Rev. B **94**, 155110 (2016).

[131] D. J. Luitz, N. Laflorencie, and F. Alet, Many-body localization edge in the random-field Heisenberg chain, Phys. Rev. B **91**, 081103 (2015).

[132] N. F. Mott, *Metal-Insulator Transition* (Taylor and Francis, London, 1974).

[133] H. Braganca, M. C. O. Aguiar, J. Vucicević, D. Tanasković, and V. Dobrosavljević, Anderson localization effects near the Mott metal-insulator transition, Phys. Rev. B **92**, 125143 (2015).

[134] G. Martinez and P. Horsch, Spin polarons in the t-J model, Phys. Rev. B **44**, 317 (1991).

[135] P. Wróbel, W. Suleja, and R. Eder, Spin-polaron band structure and hole pockets in underdoped cuprates, Phys. Rev. B **78**, 064501 (2008).

[136] K. Wohlfeld, M. Daghofer, A. M. Oleś, and P. Horsch, Spectral properties of orbital polarons in Mott insulators, Phys. Rev. B **78**, 214423 (2008).

[137] P. Wróbel and A. M. Oleś, Ferro-Orbitally Ordered Stripes in Systems with Alternating Orbital Order, Phys. Rev. Lett. **104**, 206401 (2010).

[138] J. Bała and P. Horsch, Spin-orbital physics in the optical conductivity of quarter-filled manganites, Phys. Rev. B **72**, 012404 (2005).

[139] P. Wróbel, R. Eder, and A. M. Oleś, Optical conductivity due to orbital polarons in systems with orbital degeneracy, Phys. Rev. B **86**, 064415 (2012).

[140] J. van den Brink, P. Horsch, and A. M. Oleś, Photoemission Spectra of $LaMnO_3$ Controlled by Orbital Excitations, Phys. Rev. Lett. **85**, 5174 (2000).

[141] W. Brzezicki, M. Daghofer, and A. M. Oleś, Mechanism of hole propagation in the orbital compass models, Phys. Rev. B **89**, 024417 (2014).

[142] K. Bieniasz, M. Berciu, M. Daghofer, and A. M. Oleś, Green's function variational approach to orbital polarons in $KCuF_3$, Phys. Rev. B **94**, 085117 (2016).

[143] J. Zaanen and A. M. Oleś, Carriers binding to excitons: Crystal-field excitations in doped Mott-Hubbard insulators, Phys. Rev. B **48**, 7197 (1993).

[144] M. W. Kim, J. H. Jung, K. H. Kim, H. J. Lee, J. Yu, T. W. Noh, and Y. Moritomo, Spin-Orbital Pattern Dependent Polaron Absorption in Manganites, Phys. Rev. Lett. **89**, 016403 (2002).

[145] K. Yamauchi and S. Picozzi, Mechanism of Ferro-electricity in Half-Doped Manganites with Pseudocubic and Bilayer Structure, J. Phys. Soc. Jpn. **82**, 113703 (2013).

[146] P. Dougier and P. Hagenmuller, Evolution des propriétés cristallographiques, electriques et magnétiques au sein du système $La_{1-x}Sr_xVO_3$, J. Solid State Chem. **15**, 158 (1975).

[147] N. F. Mott, Doped antiferromagnetic insulators : a model for high temperature superconductivity, J. Phys. (France) **50**, 2811 (1989).

[148] P. Horsch and W. von der Linden, On dielectric response and quasiparticles in semiconductors and insulators, Phys. Scr. **38**, 613 (1988).

[149] M. Pollak, Extension of Anderson's localization theory to interacting systems, J. Phys.: Conf. Ser. **376**, 012012 (2012).